Seismic velocity constraints on the material properties that control earthquake behavior at the Quebrada-Discovery-Gofar transform faults, East Pacific Rise

Emily Roland,[1,2] Dan Lizarralde,[3] Jeffrey J. McGuire,[3] and John A. Collins[3]

Received 2 May 2012; revised 10 September 2012; accepted 22 September 2012; published 17 November 2012.

[1] Mid-ocean ridge transform faults (RTFs) vary strongly along strike in their ability to generate large earthquakes. This general observation suggests that local variations in material properties along RTFs exert a primary control on earthquake rupture dynamics. We explore these relationships by examining the seismic structure of two RTFs that have distinctly different seismic coupling. We determine the seismic velocity structure at the Gofar and Quebrada faults on the East Pacific Rise (EPR) using P wave traveltime tomography with data from two active-source wide-angle refraction lines crossing the faults. We image low-velocity zones (LVZs) at both faults, where P wave velocities are reduced by as much as 0.5–1.0 km/s (∼10–20%) within a several kilometer wide region. At the Gofar fault, the LVZ extends through the entire crust, into the seismogenic zone. We rule out widespread serpentinization as an explanation for the low velocities, owing to the lack of a corresponding signal in the locally measured gravity field. The reduced velocities can be explained if the plate boundary region is composed of fault material with enhanced fluid-filled porosity (1.5–8%). Local seismic observations indicate that the high-porosity region lies within a ∼10 km long portion of the fault that fails in large swarms of microearthquakes and acts as a barrier to the propagation of large (M ∼ 6.0) earthquakes. Tomographic images of fault structure combined with observed earthquake behavior suggest that EPR transform segments capable of generating large earthquakes have relatively intact gabbro within the seismogenic zone, whereas segments that slip aseismically or via earthquake swarms are composed of highly fractured, ≥2 km wide damage zones that extend throughout the crust.

Citation: Roland, E., D. Lizarralde, J. J. McGuire, and J. A. Collins (2012), Seismic velocity constraints on the material properties that control earthquake behavior at the Quebrada-Discovery-Gofar transform faults, East Pacific Rise, *J. Geophys. Res.*, *117*, B11102, doi:10.1029/2012JB009422.

1. Introduction

[2] Heterogeneities in fault zone physical properties influence the spatial distribution and maximum size of large earthquakes. Though it has thus far proven difficult to characterize physical conditions within the seismogenic zone, diverse modes of fault slip, including large damaging earthquakes and slow slip or steady creep appear to be controlled by spatial variations in strain rate and rheology linked to material variability. Mid-ocean ridge transform faults (RTFs) represent an advantageous tectonic environment for exploring how material heterogeneity and fault zone architecture (including fault width and depth extent, fracture characteristics, porosity and permeability, etc.) influence earthquake rupture mechanics. Relative to other tectonic regimes, oceanic transforms are geometrically simple, with average slip rates that are well characterized by plate spreading velocities, and they occur in young oceanic lithosphere that is generally less compositionally heterogeneous compared to convergent plate boundaries or continental strike-slip faults. Based on laboratory experiments and seismicity observations, the rheology of the oceanic lithosphere is primarily controlled by temperature. Gabbro exhibits velocity-weakening behavior at temperatures less than 500°C [*He et al.*, 2007] and peridotite is velocity weakening at temperatures less than 600°C [*Boettcher et al.*, 2007]. Accordingly, in studies of oceanic transform fault earthquake behavior, the seismogenic area is commonly estimated using thermal models as the area shallower than the 600°C isotherm [*Wilcock et al.*, 1990; *Abercrombie and Ekstrom*, 2001; *Braunmiller and Nábělek*, 2008; *Roland et al.*, 2010]. However, consistently

[1]MIT-WHOI Joint Program, Massachusetts Institute of Technology, Cambridge, Massachusetts, USA.
[2]Now at Alaska Science Center, U.S. Geological Survey, Anchorage, Alaska, USA.
[3]Department of Geology and Geophysics, Woods Hole Oceanographic Institution, Woods Hole, Massachusetts, USA.

Corresponding author: E. Roland, Alaska Science Center, U.S. Geological Survey, 4210 University Dr., Anchorage, AK 99508, USA. (eroland@usgs.gov)

0148-0227/12/2012JB009422

low values of seismic coupling inferred for transforms based on global observations [*Bird et al.*, 2002; *Boettcher and Jordan*, 2004] indicate that a purely temperature-dependent rheology is unable to accurately predict the maximum size of earthquakes or the total seismic moment release on RTFs.

[3] Recently, the observation that large East Pacific Rise (EPR) and Juan de Fuca Ridge transform earthquakes occur quasiperiodically on overlapping fault patches has provided evidence that seismogenic segments of oceanic transform faults are separated by stationary, velocity-strengthening rupture barriers [*McGuire*, 2008; *Boettcher and McGuire*, 2009]. Based on centroid locations from surface waves of large RTF earthquakes throughout the past ~20 years, it appears that discrete fault segments consistently do not permit propagation of large main shock ruptures, and instead release stress through aseismic creep transients, swarms of smaller seismic events or a combination of the two [*Roland and McGuire*, 2009; *McGuire et al.*, 2012]. Together, low seismic coupling and earthquake rupture patterns at oceanic transforms signify strong spatial variations in fault frictional properties [*Boatwright and Cocco*, 1996; *Marone*, 1998; *Kaneko et al.*, 2010] that are likely influenced by fault structure and/or material variability, rather than temperature alone.

[4] The link between fault zone physical properties, structure, and slip behavior has been recognized in laboratory experiments as well as in characterizations of fault properties from field-based and geophysical studies. Laboratory friction experiments indicate that the critical slip distance (D_c), over which strength breaks down during earthquake nucleation, may be larger for faults with thick gouge zones [*Marone and Scholz*, 1988; *Marone and Kilgore*, 1993; *Marone et al.*, 2009], making it more difficult to generate large earthquakes within margins of highly fractured material. This relationship is roughly consistent with the observation that unstable slip during earthquakes tends to be restricted to depths greater than the surficial low-velocity zone associated with weak unconsolidated sediments [*Shearer*, 2002; *Lewis et al.*, 2007; *Wei et al.*, 2009]. A recent study of deformation within a subduction zone mélange suggests that some faults exhibit spatially variable rheology and strain rate and the dominant seismic style may be a function of the relative role of weak versus competent lithologies, the matrix geometry within the shear zone, and the overall degree of material heterogeneity [*Fagereng and Sibson*, 2010]. Structural complexity of fault zones that sustain distributed shear or multimode slip mechanisms should be apparent in macroscale investigations of fault structure using seismic imaging tools. Geophysical observations of fault zone elastic properties have been linked to observed styles of fault slip behavior along continental transform faults. Examples of this include the deficit of coseismic slip identified within the shallow low-velocity layer, exhibited by many M_w 6–7 strike-slip earthquakes [*Fialko et al.*, 2005] and the collocation of M 6 rupture zones with patches of high seismic wave speeds at the Parkfield section of the San Andreas Fault [*Michael and Eberhart-Phillips*, 1991; *Thurber et al.*, 2006]. Collectively, these observations indicate a relationship between the presence of low seismic velocity material and the mechanisms of strain accommodation. Targeted geophysical imaging experiments should thus be capable of illuminating characteristics of fault zone structure that signify mechanical variability.

[5] Past seismic and petrologic investigations at RTFs in the Atlantic and Pacific have identified compositional and material property variations that could be expected to influence seismic behavior [*Bonatti*, 1978; *Tréhu and Purdy*, 1984; *Calvert and Potts*, 1985; *Detrick et al.*, 1993; *Van Avendonk et al.*, 1998, 2001]. In the Atlantic, numerous seismic investigations published in the 1980s identified fault zone structure at slow slipping transform faults characterized by a wide zone of reduced seismic velocities. In some cases, observed low-velocity zones at transforms are accompanied by evidence for significantly thinned crust, attributed to alteration of the upper mantle and serpentinite diapirism [*Detrick et al.*, 1993]. The few seismic refraction studies that exist for Pacific RTFs [*Bonatti*, 1978; *Tréhu and Purdy*, 1984; *Van Avendonk et al.*, 2001] have found fault zone compressional wave velocities that are reduced compared to normal oceanic crust. These low-velocity zones have been interpreted as areas of intense fracturing and hydrothermal alteration associated with strike-slip motion along the active fault trace that extends throughout most of the crust. However, previous seismic imaging studies on EPR transforms were designed primarily to characterize tectonic processes that influence the morphology and geometry of the ridge transform environment and have thus far not focused on relating structural and material properties of these faults to earthquake processes.

[6] Here, we present results of tomographic inversions for the P wave velocity structure across neighboring EPR transform faults that demonstrate contrasting seismic behavior. The Quebrada-Discovery-Gofar (QDG) fault system (Figure 1), just south of the equator, offsets the EPR in a series of three, fast slipping transforms (141 mm/yr, based on NUVEL-1 [*DeMets et al.*, 1990]). Based on teleseismic and hydroacoustic observations of earthquake behavior over the past ~20 years, segments of the Gofar and Discovery faults sustain M_w 5.3–6.2 earthquakes on overlapping rupture patches roughly every 5 years, while only one M_w 5.5 earthquake has occurred in the vicinity of Quebrada [*McGuire*, 2008]. This behavior signifies a distinct contrast along strike in the mechanical properties of the seismically active faults, as well as a variation in the overall degree of seismic coupling at each of the individual faults within the QDG system. In 2008, as a part of the QDG Active-Passive Transform Fault Experiment, two active-source, wide-angle refraction lines were acquired, one across the westernmost segment of the Gofar fault (G3) and one across the easternmost segment of the Quebrada fault (Q1; Figure 1). We use 2-D P wave traveltime tomography to characterize the seismic velocity structure across these fault segments. We compare the resulting structural images and estimates of material properties with the seismogenic behavior of these faults, including seismicity recorded by the 1 year long deployment of a 40 station OBS array and the long-term teleseismic history of large-magnitude events. By combining results from seismic imaging with fault rupture patterns (i.e.,

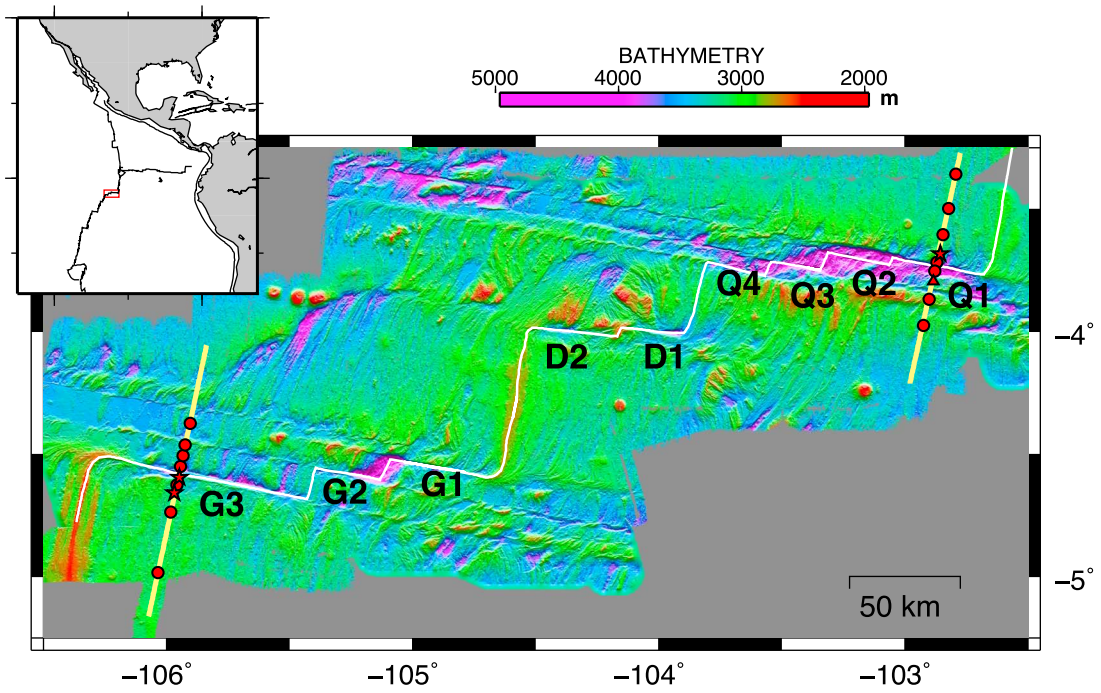

Figure 1. Bathymetric map of the Quebrada-Discovery-Gofar (QDG) fault system. Inset map shows the regional location of the transform offset on the southern East Pacific Rise. White line shows the plate boundary as indicated by pseudo side-scan backscatter [*Pickle et al.*, 2009], and yellow lines show the locations of two wide-angle refraction lines, crossing the G3 segment of the Gofar fault and the Q1 segment of the Quebrada fault. Red circles show the locations of short-period ocean bottom seismographs (OBS) and red stars and triangle show the locations of four OBS (broadband and short-period, respectively), deployed as part of the passive-source experiment that also recorded refraction data used in this study. Instrument/station numbers referred to in the text at both lines are shown in Figure 3.

the propensity for large-magnitude earthquake rupture versus aseismic slip and microseismicity), we correlate the details of fault slip behavior on Gofar and Quebrada with insight into the physical conditions at discrete segments of the RTFs that influence their mechanical behavior.

2. Tectonic Setting and Data Acquisition

[7] The QDG faults offset the EPR by 400 km between 3.5°S and 5°S. Each fault zone is broken up into multiple secondary active segments, separated by short intratransform spreading centers (ITSCs) that range in length from 5 to 16 km (Figure 1). The individual active fault segments were named by *Searle* [1983] following the first detailed side-scan sonar reconnaissance study of the QDG system. Quebrada is composed of four segments, designated Q1–Q4 from east to west; Discovery has two segments, D1 and D2; and Gofar has three active segments, G1–G3. At each fault, the active fault trace (Figure 1, white line), as indicated by pseudo side-scan backscatter [*Langmuir and Forsyth*, 2007; *Pickle et al.*, 2009], is located within a transverse valley that is relatively narrow at the Gofar and Discovery faults (∼5 km) and becomes broader and deeper at Quebrada [*Searle*, 1983].

[8] As part of a larger experiment to investigate earthquake rupture behavior at the QDG fault system, in April 2008 two active-source wide-angle refraction lines were collected, roughly perpendicular to the Gofar and Quebrada faults. The refraction lines crossed the ∼100 km long G3 fault 60 km from its eastern end and the ∼40 km long Q1 fault 20 km from its eastern end. Hereafter, the Gofar and Quebrada seismic lines will be referred to as the G3 and Q1 lines, respectively. Due to the exceptionally fast spreading rate of the EPR at this location, these faults occur in relatively young oceanic crust. Assuming a half slip rate of 7 cm/yr, crust on the south side of the G3 transect is ∼0.58 Ma and increases with distance from the fault on the north side (as crust is created at progressively more northern spreading centers) from ∼0.86 Ma near the transform to ∼2 Ma at the far northern end of the seismic line. Crust on the north side of the Q1 line is ∼0.28 Ma, while crust south of the transform ranges in age from ∼0.28 Ma near the transform to 1.42 Ma at the far southern end of the transect.

[9] The seismic source for the refraction experiment was the 36-element, 6600 cubic inch air gun array of the R/V *Marcus G. Langseth* (cruise ID MGL0808). The parallel 125 km long G3 and 107 km long Q1 lines were acquired during 5 days of shooting. At each line, shots were fired at 100 m spacing along the central 50 km section centered on the fault and at a wider spacing of 150 m along the outer 25+ km sections. Eight four-channel (three-component seismometer and hydrophone) short-period ocean bottom seismographs (OBS) designed by Woods Hole Oceanographic Institution (WHOI) from the Ocean Bottom Seismometer Instrument Pool (OBSIP) recorded crustal and upper mantle

refractions and Moho reflections. These OBSs were deployed at roughly 10 km spacing perpendicular to the active fault traces. Associated with the QDG Active-Passive Transform Fault Experiment, the G3 and Q1 surveys occurred during a yearlong passive deployment of an array of broadband OBSs (BBOBS) that recorded local seismicity at the QDG faults. Ten of these BBOBS designed by WHOI also incorporated strong motion accelerometers in order to record large-magnitude local earthquakes and are distinct from the OBSIP. At Gofar, two BBOBSs associated with the passive experiment were located roughly along the refraction line within 20 km of the fault. At Quebrada one BBOBS and one short-period passive array instrument were located roughly along the refraction line. These instruments (Figure 1, red stars and triangle) also recorded active-source arrivals during the G3 and Q1 shooting, and these data are included in the tomographic inversions presented here.

[10] High-quality compressional wave seismograms were recorded on the vertical component seismometer and the hydrophone at each of the 10 stations on the two lines. The short-period and broadband instruments sampled at rates of 200 and 50 Hz, respectively. Vertical component seismogram data were used to pick first-arrival times of crustal refractions, upper mantle refractions and Moho reflections (Pg, Pn, and P_MP, respectively), except at two stations (G3-6 and G3-4) where the seismometers appear to have been poorly coupled to the seafloor, and where instead data from the hydrophone channel were used for picking. Data were band-pass filtered between 3 and 15 Hz using a minimum-phase Butterworth filter, and predictive deconvolution was applied to reduce reverberative noise. For phase picking, record sections were reduced to 7 km/s and refraction and reflection arrivals were picked by hand. In order to account for any static offset in picked traveltimes resulting from a residual instrument response not accounted for in the preliminary processing of the OBS data, water column direct-arrival times were also picked and compared to the predicted arrival time at each station assuming the correct station location and a water velocity of 1.5 km/s. At stations G3-6 and G3-p8 the predicted water column direct arrivals showed a systematic delay with respect to the observed arrival times, and a correction was made to refraction and reflection phase picks of less than +0.2 s to account for the offset.

[11] High-quality first arrivals were recorded at all stations, but the substantial bathymetric relief across the Gofar and Quebrada faults made it difficult in some instances to distinguish phases associated with particular layering, such as seismic Layers 2 and 3, as well as the transition from Pg to Pn at far offsets and, in many cases, a distinct P_MP phase. Pn arrivals were only picked with high confidence at a few instruments. The few Pg/Pn crossovers in this data set occur at offsets between 32 and 35 km. The presence of clear P_MP mantle reflections was also variable along both of the lines. Particularly along the Q1 line, P_MP appears to rarely propagate through the fault zone. At both the G3 and Q1 lines, 9 P_MP branches were picked and used in the inversions. Where P_MP is present, it was picked at offsets that ranged between 15 and 35 km and, with a few exceptions, approached the first arrival at offsets of roughly 23–26 km.

[12] Several measures were taken to verify the Pg, Pn, and P_MP picks. We used reciprocity to confirm the consistency of picked phases at multiple stations by comparing arrival times of phases that shared similar raypaths at reversed source/receiver locations. To guide arrival picking, particularly of P_MP, we also compared the observed data to synthetic wavefields calculated using a pseudospectral approach [*Kosloff and Baysal*, 1982]. We estimated conservative traveltime pick uncertainties, guided in part by the dominant period of the first-arrival phase and in part by a subjective estimation of our confidence in the phase picks. We assigned uncertainties of 20 ms to all Pg and Pn picks and higher values of 40 ms for P_MP.

[13] The general pattern of first-arrival traveltimes is diagnostic of deeper crustal structure. This is apparent in data from OBS G3-3, shown in Figure 5. The arrivals at positive offsets, shooting to the south (left in Figure 1) away from the fault, are fairly typical of oceanic crust. First arrivals between 3 and 10 km source-receiver offset are from oceanic Layer 2. The transition to Layer 3 refractions is marked by a clear change in first-arrival slope at ~10 km offset, and the apparent velocity of the Layer 3 phase Pg remains nearly constant at ~7 km/s from 10 to 50 km offset. Neither the P_MP phase nor Pn are obvious on the profile. At negative offsets, heading toward the fault (and to the right in Figure 1), note that the seafloor remains more or less flat out to −15 km offset, to the edge of the fault zone. Despite this, first arrivals for the Layer 2 phase are slower than for shots to the south, and there is no obvious transition to a higher-velocity phase typical of oceanic Layer 3 as observed at 10 km offset in the opposite direction. This indicates a progressive deepening of slow upper crustal material as the fault is approached from the south. From −16 to −23 km offset, the first arrivals are markedly delayed by the bathymetric low of the active fault zone. Between −23 and −32 km offset (model km 71–80), however, the seafloor is nearly flat and at approximately the same depth as the seafloor to the south at the same offset range. The first-arrival phase between −23 and −32 km offset is a refraction that has passed through the fault zone at midcrustal to lower crustal depths. Comparison of the arrival time of this phase with the Pg phase at 23–30 km positive offset, to the south, which has not gone through the fault zone, provides some measure of the amount of traveltime delay associated with the fault zone in the lower crust. For example, the arrival time of the Pg phase at −29 km offset is ~2.9 s, and the arrival time of the Pg phase at +29 km offset is ~2.5 s. This delay in traveltime (in this case ~0.4 s) of rays passing through the fault relative to those that do not is observed in one form or another on all of the profiles, and it is the primary signal that is reconstructed by the tomographic inversion to image the velocity structure of the fault zone.

3. Ray Tracing and Tomographic Inversion

[14] The tomographic method fundamentally involves three steps: specification of an initial velocity model, ray tracing (the forward problem), and the tomographic inversion to update the model as required by the data. In this study we utilize a seismic tomography code first developed by H. Van Avendonk and recently updated by A. Harding at Scripps Institution of Oceanography (SIO) that follows the basic strategy outlined by *Van Avendonk et al.* [1998, 2004]. This code incorporates the graph method ray tracing scheme

(or shortest path method) [*Moser et al.*, 1992a; *Toomey et al.*, 1994; *Van Avendonk et al.*, 1998]. The tomographic inversion is implemented in the form of a damped least squares minimization of the traveltime residuals with smoothing constraints to regularize the inverse problem.

[15] Our initial velocity model is parameterized as a two-dimensional (2-D) grid of regularly spaced nodal points with assigned slowness values. The location of interfaces separating subhorizontal model layers are assigned at the same horizontal nodal points as slowness values but can have independent depth values. With this parameterization, both the location of an interface and the amplitude of a slowness jump across an interface may be changed during the inversion process, along with the slowness or slowness gradient within a given layer [*Van Avendonk et al.*, 2004].

3.1. Graph Method of Ray Tracing

[16] We use a ray-tracing scheme that employs the graph method to solve the forward problem with both a high degree of accuracy and relatively little computational cost. The graph method is used to approximate raypaths by connecting straight-line segments between neighboring grid points. In this way, the cumulative traveltime is propagated from a source location to all other points in space, and the true path is determined to be the global minimum time path, in agreement with Fermat's principal. Here, following *Moser et al.* [1992b], *Toomey et al.* [1994], and *Van Avendonk et al.* [1998], the grid search is limited to the forward propagation direction, termed the *forward star*. For this study, we employ a forward star with a minimum angle of 0.5° specified between search directions. We consider 6 nodes in the x direction and 12 nodes in the z direction during the graph method search; this preferential search in the downward direction is effective in environments where the vertical velocity gradient dominates the horizontal gradient [*Korenaga et al.*, 2000], as would be expected throughout most of the oceanic lithosphere.

[17] The graph method is particularly well suited for marine wide-angle refraction data sets, as it allows ray tracing to be implemented through models with complex seafloor topography, like that in the vicinity of the mid-ocean ridge and transform domain. Adopting the graph method in this study has also been advantageous due to its ability to find first-arrival traveltimes of nongeometric diffracted waves [*Van Avendonk et al.*, 1998], like those that would be expected to occur within the kilometer-scale relief of the transform valley. The minimum error of calculated traveltimes is dependent on the grid spacing. We chose a grid spacing of 50 m in both the vertical and horizontal directions, which is sufficiently fine so as to determine an accurate minimum traveltime. This choice was tested by comparing traveltimes determined using the graph method to those calculated using an analytical traveltime equation through a 1-D vertical velocity gradient [*Shearer*, 1999]. Using 50 m grid spacing, errors in the graph method calculations, as compared to the analytical traveltimes were much less than estimated pick errors.

3.2. Tomographic Inversion

[18] The inversion approach used here follows closely that outlined by *Van Avendonk et al.* [1998, 2004]. We again utilize code for the inversion developed and maintained by A. Harding at SIO. This approach solves the damped least squares problem to minimize an objective function for the preferred model slowness perturbation based on a set of scaled traveltime residuals. In general, tomographic inversions rely on a linear set of equations derived from Fermat's principal, which relate a variation in traveltime to a variation in model slowness along the stationary raypath, p_i. The traveltime residual, δT_i, can thus be expressed as a linear combination of a slowness perturbation, δu, to a predefined slowness model along p_i and a change in the depth of a layer boundary, δr_k at each layer k through which the ray travels [*Van Avendonk et al.*, 2004]:

$$\delta T \approx \int_{p_i} \delta u(x,z)ds + \sum_k \Gamma_{i,k}(x)\delta r_k(x). \quad (1)$$

Applying equation (1) to the full suite of traveltime picks leads to a set of linear equations that is solved in the least squares inversion. First-arrival refraction and reflection traveltime differences determined for the picked phases and the forward ray-traced arrival times are scaled by the pick error and combined in an $n \times 1$ vector of scaled traveltime residuals. This data vector is related to the Frechét derivative matrix and the unknown slowness perturbation vector, which is normalized by the slowness of the reference model, to arrive upon a matrix equation:

$$d = Gm, \quad (2)$$

in which d is composed of the scaled traveltime residuals, G is the Frechét derivative matrix and m is the normalized slowness perturbation vector. In order to calculate accurate graph method raypaths, we choose a grid spacing that is finer than expected velocity variations. Consequently, it is likely that the least squares matrix equation above is over parameterized, with many more model grid points than traveltime picks. Following *Van Avendonk* [1998], where the model is unconstrained by data, a smooth model is assumed by imposing roughness penalties, F_{s_1} and F_{s_2}, that are functions of the first and second derivatives of the model slowness:

$$F_{s_{1,2}} = (P_1, P_2) \int \left[L_H^2 \left(\frac{d^{1,2}u}{dx^{1,2}} \right)^2 + L_V^2 \left(\frac{d^{1,2}u}{dz^{1,2}} \right)^2 \right]. \quad (3)$$

The specified length scales of smoothing, L_H and L_V, and the smoothing regularizations, P_1 and P_2 control the smoothing penalty functions, and we choose values for these parameters to facilitate a solution that is consistent with the expected physical environment. In many tomographic problems, it is reasonable to assume that the length scale of heterogeneity is greater in the horizontal versus the vertical direction, and so the aspect ratio L_H/L_V is large (usually >10). Here, based on the horizontal dimensions of dramatic seafloor morphology in the vicinity of the active transform, we have reason to believe that the aspect ratio of heterogeneity is much smaller. As such, we assume an L_H/L_V of 2 for the inversions on both the G3 and Q1 lines. The strength of the first and second derivative smoothing penalties, controlled by P_1 and P_2, are changed frequently during progressive inversion iterations. The choice of preferred values for these first and second derivative regularizations is made in a

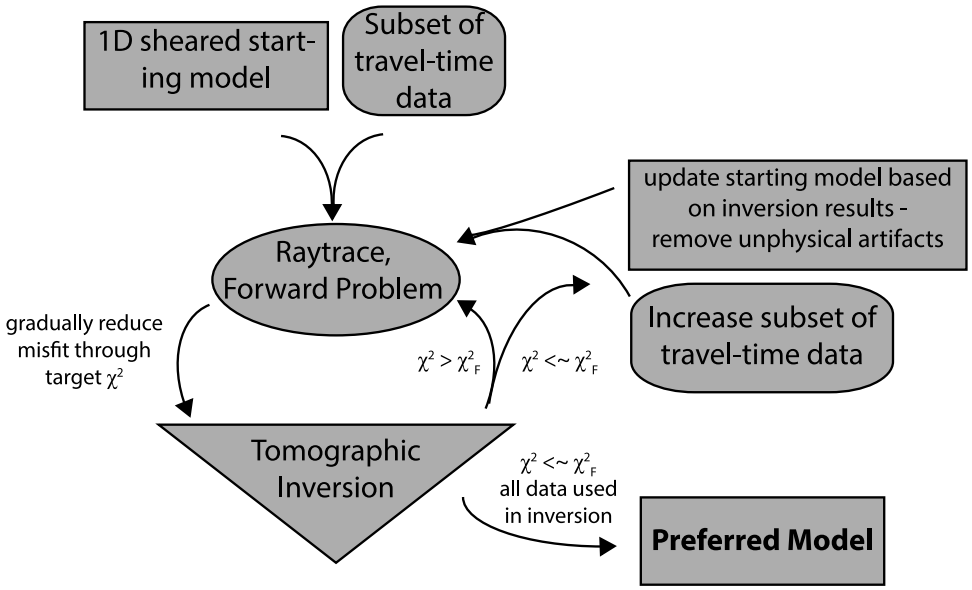

Figure 2. Schematic diagram that demonstrates the forward ray tracing and tomographic inversion approach we perform to arrive upon our preferred velocity models. We use a tomographic inversion code developed by H. Van Avendonk and A. Harding that uses methodology presented by *Van Avendonk et al.* [2001, 2004].

largely subjective manner. At each inversion iteration, P_1 and P_2 are selected with the goal of reducing the occurrence of nonphysical artifacts, such as ray streaks and high-frequency lateral oscillations, while also not oversmoothing velocity perturbations along the raypaths. Throughout the tomographic process, we typically specify P_2 to be 1.3–2.0 times greater than P_1. Early in the tomographic process, when the starting model is far from the true velocity structure, large first and second derivative regularization values are specified, and the strength of smoothing is reduced as model error is decreased in progressive inversion iterations.

[19] Especially for problems with large initial traveltime residuals, applying damping to the least squares inversion maintains the assumption of linearity expressed in equation (1) by keeping the raypaths from changing too quickly (i.e., requiring that the traveltime is stationary with respect to $p_i(u)$ and $p_i(u + \delta u)$). In our inversion process, the rate at which slowness perturbations are incorporated into the model is controlled by damping values, which balance the improvement of data fit with the norm of the model perturbation. Damping is also applied to changes in the depth of a specified reflector interface and changes in the slowness jump across the interface. The damped least squares approach penalizes the magnitude of these perturbations via a damping penalty that is a function of the magnitude of the model perturbations and specified damping coefficients. These values together control the strength of the damping applied, and how slowness perturbations are distributed during the initial stages of residual traveltime minimization.

[20] During the inversion process, we choose regularization values for slowness changes within individual layers that, similar to the smoothing operators, are high in early inversions, and then are decreased as model predictions improve with iterative updates. As we discuss in more detail in section 3.3, we begin our tomographic process by inverting only for traveltime residuals associated with shallow crustal phases that do not extend to the lower crust. As such, early in the inversion process, we insure that the Moho slowness jump and depth do not change by specifying high slowness jump and reflector depth damping regularizations. As we incorporate more traveltime data, these values are also reduced, allowing some change to the Moho interface as required by the P_MP and Pn traveltime picks.

3.3. Solution Procedure

[21] Raypaths determined during the forward problem are strongly dependent on the initial velocity model. It is thus advantageous to choose an initial model that emulates the real local velocity heterogeneity as closely as possible. In order to accomplish this without biasing our starting model with preimposed fault zone structure, we employed an iterative approach to the tomographic method outlined above in which we alternate between the forward and inverse problems, first using a small subset of the traveltime data within the most well resolved portion of the model space, then updating the starting model appropriately based on the inversion results. Subsequent rounds of forward and inverse calculations are conducted using the new starting model and more traveltime data. We thus begin by inverting for the shallow structure within the center of the model space (where station spacing is slightly finer) using only close range Pg arrivals, and incrementally incorporate deeper and more wide-ranging Pg and Pn picks, capable of resolving the midcrust–lower crust, and eventually P_MP arrivals that constrain the lower crustal velocities and the Moho. We repeat this multistep approach to the tomographic inversion process until the starting model is close enough to the true model that only a few additional iterations of the nonlinear inversion result in a model with an acceptable level of

traveltime fit. In Figure 2, we present a schematic diagram that demonstrates the strategy we perform to arrive upon our preferred velocity models.

[22] Following a forward calculation, total misfit between the modeled and observed data is calculated as a χ^2 value, defined as

$$\chi^2 = \sum_{n=1}^{N} \frac{\left(t_{n,ray} - t_{n,pick}\right)^2}{\sigma_n^2}. \quad (4)$$

This number is used to inform the target misfit level for the following inversion. As an additional strategy for limiting the amount of change allowed during an inversion, we decrease the target χ^2 value gradually, starting with a target 10–20% error reduction, and then increasing the percent improvement until either unphysical artifacts are incorporated into the velocity model or we arrive upon our preferred solution. Ray "streaks," negative velocity gradients, and unrealistically high- or low-velocity patches are common features that arise in inversion results in regions of low ray coverage due to the extreme traveltime anomalies present in our starting model. Increasing smoothing constraints can sometimes mitigate this, but even a significant amount of model smoothing is insufficient if the initial velocity model is too far from the model required by the data. We avoid incorporating unphysical slowness perturbations in our final velocity model by gradually decreasing the target misfit during iterations of the forward and inverse problems. If at some point an undesirable artifact is incorporated into the model while the total error is still too high, we remove this by updating the starting model manually to remove unphysical structure from regions with poor ray coverage, and proceed with the tomographic process until an acceptable χ^2 value is achieved. In this way we arrive upon a model that is physically realistic and fits the data.

4. Inversion Results

[23] Starting models were constructed for both the G3 and Q1 transects from a 1-D velocity profile similar to those determined for young Pacific oceanic crust [*Harding et al.*, 1989; *Vera et al.*, 1990; *White et al.*, 1992]. The 1-D model was hung from high-resolution bathymetry profiles across each line, acquired from combined multibeam surveys collected at ~200 m resolution from aboard the R/V *Knorr* (cruise ID KN182–13) in 2006 [*Pickle et al.*, 2009] and improved to roughly ~100 m resolution during successive cruises on the R/V *Thomas G. Thompson* (TN214) and R/V *Marcus G. Langseth* (MGL0808) in 2008. Starting models include a flat Moho reflector specified at a depth of approximately 6 km beneath the seafloor. Models extend from the sea surface at $z = 0$ to $z = 13$ km, leading to a G3 model parameterization composed of 2953 × 261 nodes and a Q1 model composed of 2121 × 261 nodes (124.6 and 106.0 by 13 km respectively, at 0.05 km grid spacing).

[24] In total 4428 first-arrival (Pg and Pn) and 497 P_MP picks were used for the G3 tomographic inversion, and 3678 first-arrival and 528 P_MP picks were used for Q1. Negative average traveltime residuals at several of the off-fault instruments on both lines indicated that the data required a faster shallow velocity gradient than what was specified in the starting model. However, despite the moderately late prediction of traveltimes in the unfaulted shallow crust, rays that passed through the fault zone were delayed significantly, leading to dramatic positive traveltime residuals. Starting model traveltime residuals for rays passing through the 10–20 km of crust surrounding the fault were delayed as much as 0.5 s at both the G3 and Q1 lines. The largest positive traveltime residuals were recorded by instruments G3-4, G3-7, Q1-4, Q1-6 and Q1-p13 (instrument labels are shown in Figure 3), and these would have likely been larger had the starting model been more appropriate for the unfaulted crust. The starting χ^2 value for the G3 line was 55, and this was reduced to the value in the preferred final model of $\chi^2 = 1.8$ after 34 iterations. The starting χ^2 value at the Q1 line was 27, and it was reduced to the preferred model value of $\chi^2 = 2.0$ after 12 iterations. χ^2 values reflect data fit relative to the estimated errors, and so by maintaining small error estimates, the χ^2 value will be larger. The inversion process would allow for the data to be fit more completely (with smaller final χ^2 values), however we choose to maintain a level of smoothing appropriate for the length scale of heterogeneity we expect to resolve.

[25] Figure 3 displays the preferred P wave velocity models for the G3 and Q1 lines. The most striking feature apparent in both of these models is the significant low-velocity zone (LVZ) within the central fault zones. Substantially reduced P wave velocities are required to fit the traveltime data at both the Gofar and Quebrada faults. LVZs at both faults occupy a ~10 km wide region within the shallow crust that decreases in width gradually with depth. Across the G3 fault, the modeled LVZ extends throughout the entire crust, with velocities that are reduced by more than 12% within the lower crust and by as much as 25% at shallow depths. Within the shallow crust, the LVZ at the Q1 line is equally pronounced and wider laterally as compared to the G3 model. However, no substantial reduction in velocity is resolved within the lower half of the crust at Q1. As we discuss in section 5, this may reflect ray coverage as opposed to differences in the actual depth extent of the LVZ along the two faults. It is interesting to note that the broad low-velocity zones we resolve here are centered on the location of the active fault trace determined from seafloor backscatter imaging (black arrow in Figure 3), slightly offset from the deepest part of both transform valleys.

[26] Away from the central fault zones, the seismic velocity structure is generally consistent with crustal velocities determined in past seismic refraction studies of young EPR crust [*Harding et al.*, 1989; *Vera et al.*, 1990; *White et al.*, 1992]. Figure 4 shows velocity-depth profiles at different offsets along the two lines compared with velocity profiles from previous studies. Some differences are apparent in the structure of the crust generated at the "normal" EPR spreading center (southern side of the G3 line and northern side of the Q1 line), and that associated with intratransform spreading (northern side of the G3 line and southern side of the Q1 line). Additionally, lateral transverse ridges and fossil fault traces that are apparent in the bathymetry correspond to velocity heterogeneities where they intersect the G3 model at approximately 82 and 96 km offset. The same appears to be the case in the vicinity of the morphologically complex Quebrada fault, where a transform-parallel ridge and linear troughs are aligned with a less dramatic but discernible secondary low-velocity region to the south of the active fault.

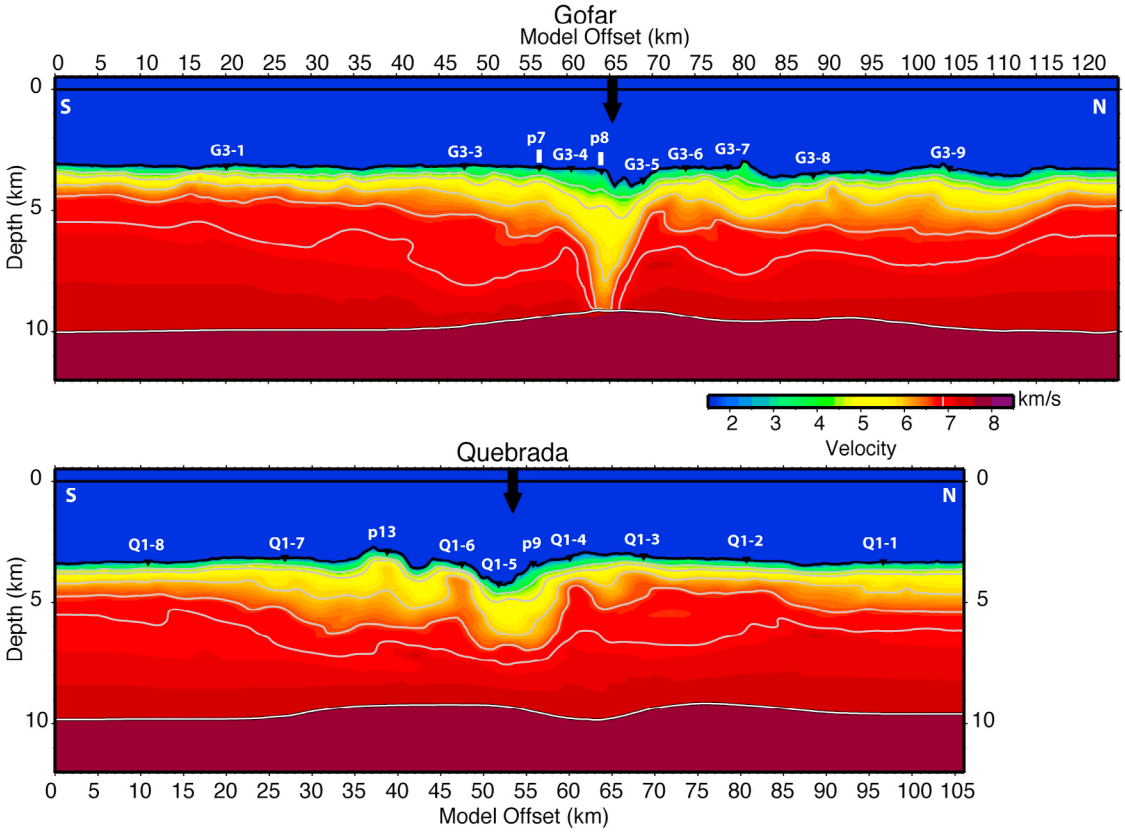

Figure 3. P wave velocity profiles determined from the (top) G3 and (bottom) Q1 wide-angle refraction data sets. Receivers located on the seafloor are shown as black triangles. All receivers are short-period OBS deployed for the refraction experiments, except for those with "p" labels, which were deployed for the yearlong passive-source experiment; p7, p8 and p9 are broadband seismometers, and p13 is a short-period seismometer. Black line located at ~7 m depth shows the location of shots (at ~100–150 m spacing). Outlined white lines show the locations of the Moho reflector as determined by our inversions. Velocity is contoured at 4.2, 5.0, 6.0, 6.6 and 7.0 km/s. Black arrows show the approximate location of the active fault from pseudo side-scan backscatter [*Pickle et al.*, 2009].

[27] Average crustal thickness across the two faults is comparable, with the Moho discontinuity occurring at a depth of approximately 6.0–6.6 km beneath the seafloor. Within the central fault zones at both G3 and Q1 the Moho shallows somewhat, which combined with the bathymetric lows within the transform valleys, leads to a thinning of the crust at the fault zone to approximately 5 km. General features of crustal thicknesses resolved here are roughly consistent with those determined in the region based on the residual mantle Bouguer anomaly derived from regional gravity data by *Pickle et al.* [2009].

5. Data Fit and Model Resolution

[28] Tomographic inversions are inherently nonunique. The capability to resolve structural features depends on the geometry of the seismic experiment and the quality of the data acquired. Furthermore, the imposed inversion correlation lengths and the long wavelength of the seismic waves that sample the subsurface lead to inversion results that are expected to be a smoothed version of the real structure. To understand how these factors should be considered in interpreting our inversion results, we evaluate our resolution in this section.

[29] In Figures 5–7 we display the observed and modeled traveltime curves along with ray diagrams for three of the Gofar stations (G3-3, G3-5, and G3-p7), and in Figures 8–10 we present similar traveltimes and ray coverage for Quebrada stations (Q1-7, Q1-4, Q1-3). Figures 5–10 illustrate the type of structure we are capable of fitting using our inversion process. Large-scale trends in traveltimes are modeled well. Data at several stations show first-arrival times of rays passing through the fault zone that are delayed by ~0.85 s, signifying slow material that produces the fault zone anomaly in our final inversion results. However, some small-scale features, like the small delay in traveltimes located at ~15 km on G3, are difficult to replicate. More importantly, regions of the model with sparse ray coverage are often sampled by phases that are difficult to pick accurately. The lower crustal structure, for example, is primarily constrained by P_MP mantle reflections, which have larger picking uncertainties and weaker velocity sensitivity than Pg phases.

[30] An indication of the sampling of velocity model nodal locations can be found by calculating the derivative weight sum (DWS). The DWS is a qualitative measure of ray

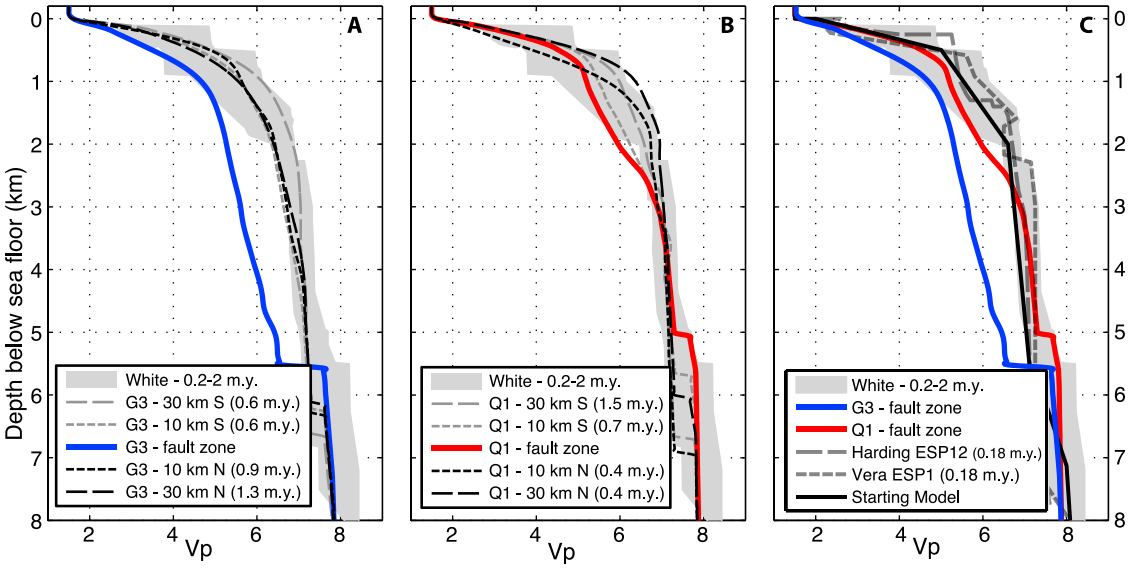

Figure 4. One-dimensional velocity-depth profiles from the Gofar and Quebrada velocity models compared to other velocity models determined for Pacific oceanic crust. (a) A 1-D velocity depth profile taken beneath the active trace of the Gofar fault (~66 km offset, blue line) compared to profiles at 10 and 30 km south (gray lines) and north (black lines) of the fault zone. The gray shaded area shows a compilation of nine profiles across normal young oceanic crust (0.2–2 Ma) modeled using synthetic seismograms [*White et al.*, 1992]. (b) Similar comparison of profiles at the Quebrada fault, with the central fault zone (offset ~52 km) shown in red. (c) The Gofar and Quebrada fault zone velocity-depth profiles compared to the starting model and to several other models for young oceanic crust determined from expanding spread profiles ESP1 near the EPR at 9°N [*Vera et al.*, 1990] and ESP12, 10 km off axis of the EPR near 12°N [*Harding et al.*, 1989].

density and is calculated by summing the influence of a model parameter on an integrated path length over all ray-paths [*Toomey and Foulger*, 1989]. In Figure 11, the DWS is displayed for the two refraction transects. Higher values of DWS in these regions indicate more well-sampled regions of the models space, although the DWS should only be used as a relative indicator of resolution, and the absolute value is not physically significant. Within the upper crust, both models are well sampled with a high density of rays, and coverage is moderately good throughout most of the central fault domain. Sections of the lower crust, however, have significantly lower DWS values, and parts of the lower crust are completely unresolved. In addition to the density of rays, coverage with crossing rays from different directions is also important for localizing the velocity perturbations. At locations within the lower crust, where there is reasonable ray coverage, there are rarely abundant crossing rays. Of particular importance to this study is the paucity of ray coverage in the lower crust beneath the Quebrada transform valley. A key difference in the modeled velocity structure of the two faults is the depth extent of the LVZ imaged within the central fault zone. The low ray coverage beneath the Quebrada fault indicates that we may be unable to determine the true depth extent of reduced velocities in the Quebrada transform domain with this data set.

[31] In order to further evaluate the tomographic inversion results, we present a series of resolution tests in Figures 12–15. These tests utilize synthetic data that is produced by forward modeling traveltimes through a 1-D model hung from the bathymetry along each line that has a velocity anomaly imposed within some portion of the model space. The ability of the tomographic inversion to reproduce the velocity anomaly using the same ray configuration and a similar inversion strategy (iterative process, smoothing and damping constraints, target error reduction, etc.) provides some insight into the resolving capabilities of these data sets. As indicated by the DWS values, our primary concern is with the resolution of any velocity heterogeneity in the lower crust and particularly lateral velocity heterogeneity associated with the fault zone. In Figures 12 and 13, results are displayed from resolution tests in which we model a 5 km wide LVZ with a 30% velocity reduction that extends throughout the entire model space. With the ray coverage available for the G3 line, the imposed velocity anomaly is resolved well throughout the crust and into the upper mantle (Figure 12). In the shallow part of the crust, the entire velocity anomaly is accurately imaged with minor lateral smoothing. At lower crustal depths (>5 km beneath the seafloor), the velocity anomaly that is reproduced is narrower and less slow than the input model. The same velocity anomaly, when modeled using the Q1 ray configuration, is reproduced well in the shallow crust but by midcrust depths (greater than ~4 km beneath the seafloor) the resolved anomaly is reduced to only a few percent (Figure 13). This result shows a lack of resolution in the lower crust at Q1 and suggests we may not be capable of imaging deep fault structure at Quebrada.

[32] In Figure 14, we display another resolution test for a narrower, 2 km wide fault zone anomaly throughout the crust at G3. Using a starting data set produced from a 30% velocity reduction in this zone, the relatively narrow low-

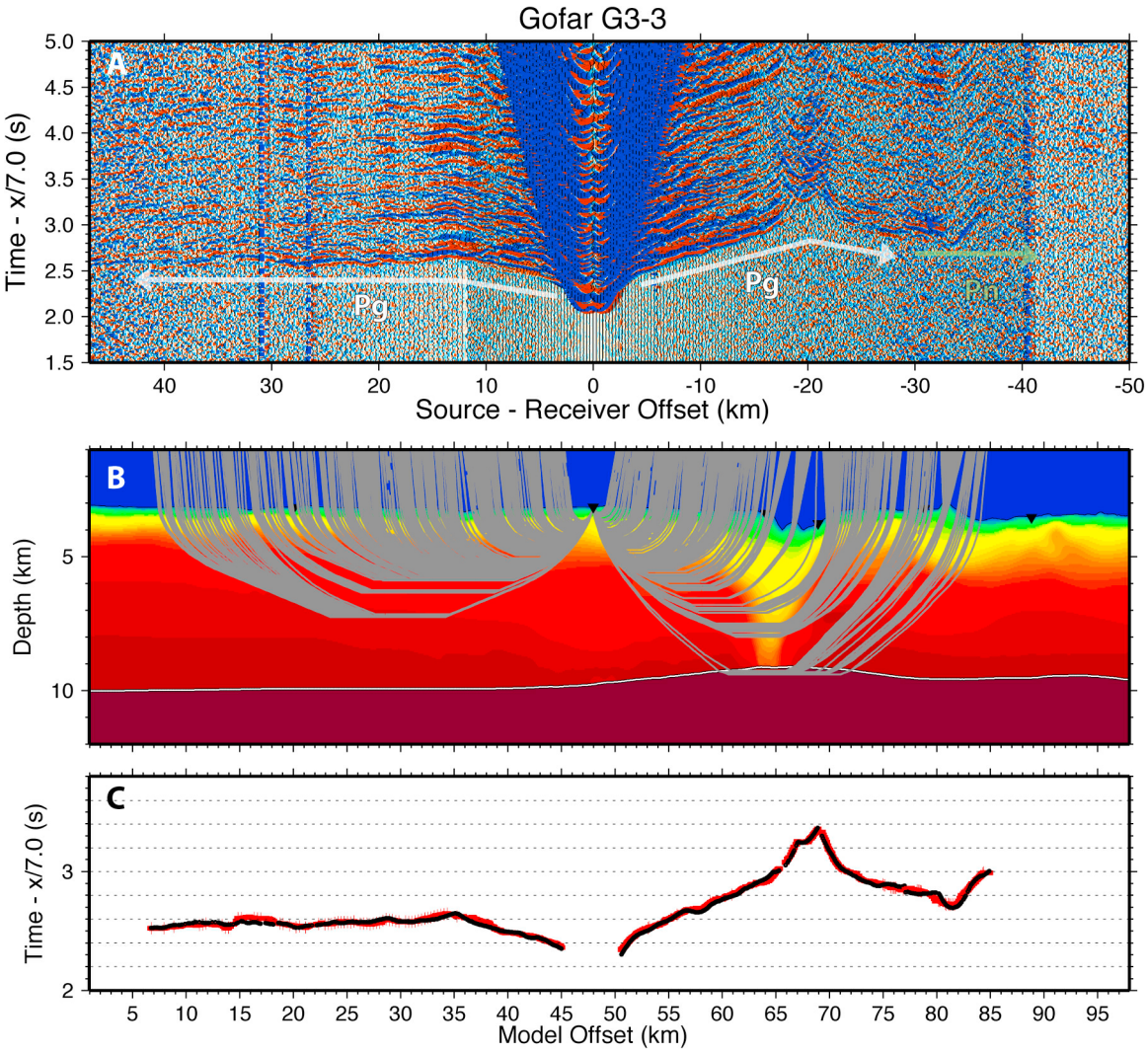

Figure 5. (a) Data recorded at G3-3, reduced at 7.0 km/s. Pg and Pn phase first-arrival times that were picked and used in the inversion are labeled here with white and green lines drawn below the actual arrival so as not to obscure data. (b) Rays traced through preferred Gofar G3 velocity model using the graph method. Velocity color scale is same as that shown in Figure 3. White line indicates Moho, and black triangles show receiver locations. (c) Pg and Pn first-arrival traveltime picks for G3-3 (red) compared to the modeled traveltimes using preferred P wave velocity model (black). Heights of modeled data points indicate the assumed traveltime pick error.

velocity anomaly is very well modeled at shallow depths, and at mid crustal depths there is only minor lateral smearing of the fault zone anomaly after the inversion. Because the LVZ is wider in our preferred velocity model at G3 than the signal produced from the 2 km wide resolution test model, especially in the shallow crust, this exercise helps to bound the minimum width and strength of the zone of low-velocity material present at Gofar. Based on this result, we expect that the true zone of low-velocity material would have to be wider than 2 km and/or more than 30% slower to produce the kind of signal we determine from our inversion.

[33] In order to assess the degree to which velocity anomalies may be smeared downward in the tomographic process, in Figure 15 we present results from a third G3 resolution test in which we model a 5 km wide, 30% reduced velocity anomaly that is confined to the upper 2 km beneath the seafloor. Results from this test are encouraging, showing that very little downward smearing occurs. As would be expected, some small degree of both lateral and vertical smoothing of the true velocity signal is visible in the resolution tests, even within the most well resolved portions of the model space. Together, these resolution tests show that a LVZ imaged in the midcrust and lower crust at G3 may be slightly exaggerated in width, but not in depth, and most likely underestimates the strength of the actual anomaly at depth.

6. Discussion

6.1. Influence of Past and Current QDG Tectonics

[34] The QDG area has experienced a complex tectonic history, resulting in a system of subparallel transform faults connected by ITSCs. A first-order feature of the seismic

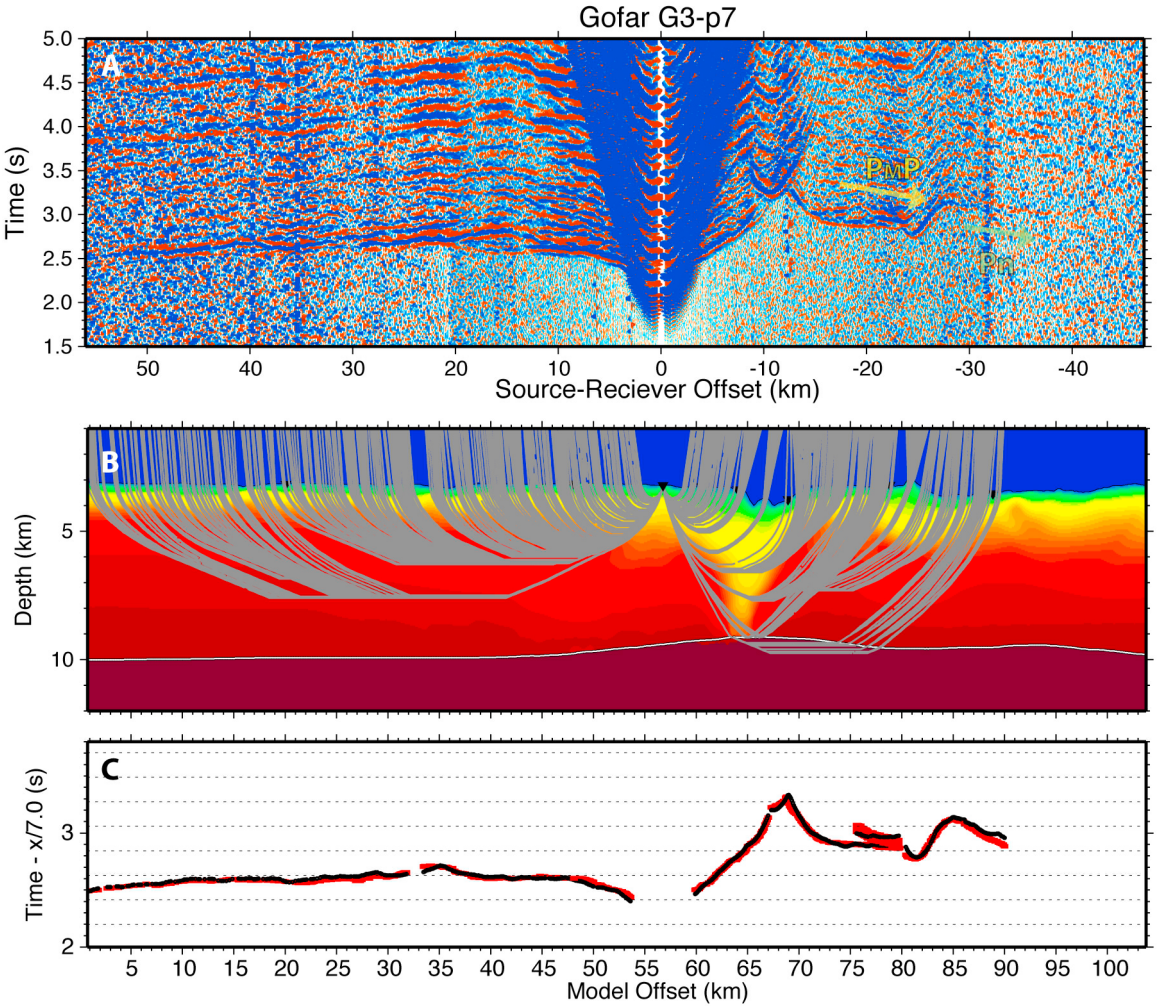

Figure 6. (a) Data, (b) ray diagram, and (c) traveltimes for station G3-p7 (for more details, see Figure 5 caption). Figure 6a also has picked P_MP and Pn phases labeled above and below the actual arrivals, respectively, so as not to obscure the data. Pg phases were also picked but are not labeled here.

velocity profiles across both the Gofar and Quebrada faults is a difference in the shallow structure of crust created at "normal" EPR spreading centers, north and south of the QDG offset, and that generated at ITSCs. Several differences in the crustal structure can be identified by comparing the velocity profiles on either side of the Gofar and Quebrada faults (Figure 4), specifically the thickness of the shallow crustal extrusive Layer 2a, and lateral velocity heterogeneity coincident with fossil fracture zones.

[35] ITSC-generated crust on the north side of the G3 fault exhibits a slower shallow velocity structure as compared to crust to the south. Seismic Layer 2A is typically identified by a shallow low-velocity layer over a sharp velocity gradient down to ~5.2 km/s [*Christeson et al.*, 1994]. Using this definition, the median Layer 2A thickness increases from ~500 m on the south side of the Gofar fault to ~700 m on the north side. Previous marine seismic experiments have noted a decrease in the thickness of Layer 2A with age [*Houtz and Ewing*, 1976; *Purdy*, 1987], thought to result from hydrothermal alteration and reduction of the bulk porosity in pillow basalts, flows, and breccia that compose the shallow oceanic crust. At the location of the G3 line, the crust north of the fault is 0.3–1.4 Myr older than crust to the south, and thus a thicker Layer 2A to the north more likely reflects a difference in the abundance of volcanic extrusives produced at the ITSC rather than age evolution of the high-porosity layer. Average Layer 2A thickness is greater in young oceanic crust created at the slow spreading Mid-Atlantic Ridge as compared to at the fast spreading EPR [*Houtz and Ewing*, 1976]. The difference in shallow crustal structure across G3 may thus be evidence for a contrast in emplacement processes at the short ITSCs, signifying a more magma-starved ridge environment. The same trend is true for Layers 2B–C, which increase in median thickness from 1.6 km south of the fault, typical for young EPR crust [*Vera et al.*, 1990], to 2.3 km to the north, assuming they are bound by the 5.2–6.8 km/s velocity contours. Combined, we see a significantly thicker Layer 2 associated with crust created at the spreading centers north of the Gofar fault than what has been identified in other refraction studies in normal EPR crust [*Harding et al.*, 1989; *Vera et al.*, 1990] without necessarily resolving an equivalent increase in total crustal thickness.

[36] Based on elemental compositions from basalts dredged at the ITSCs at QDG [*Nagle et al.*, 2009] and other

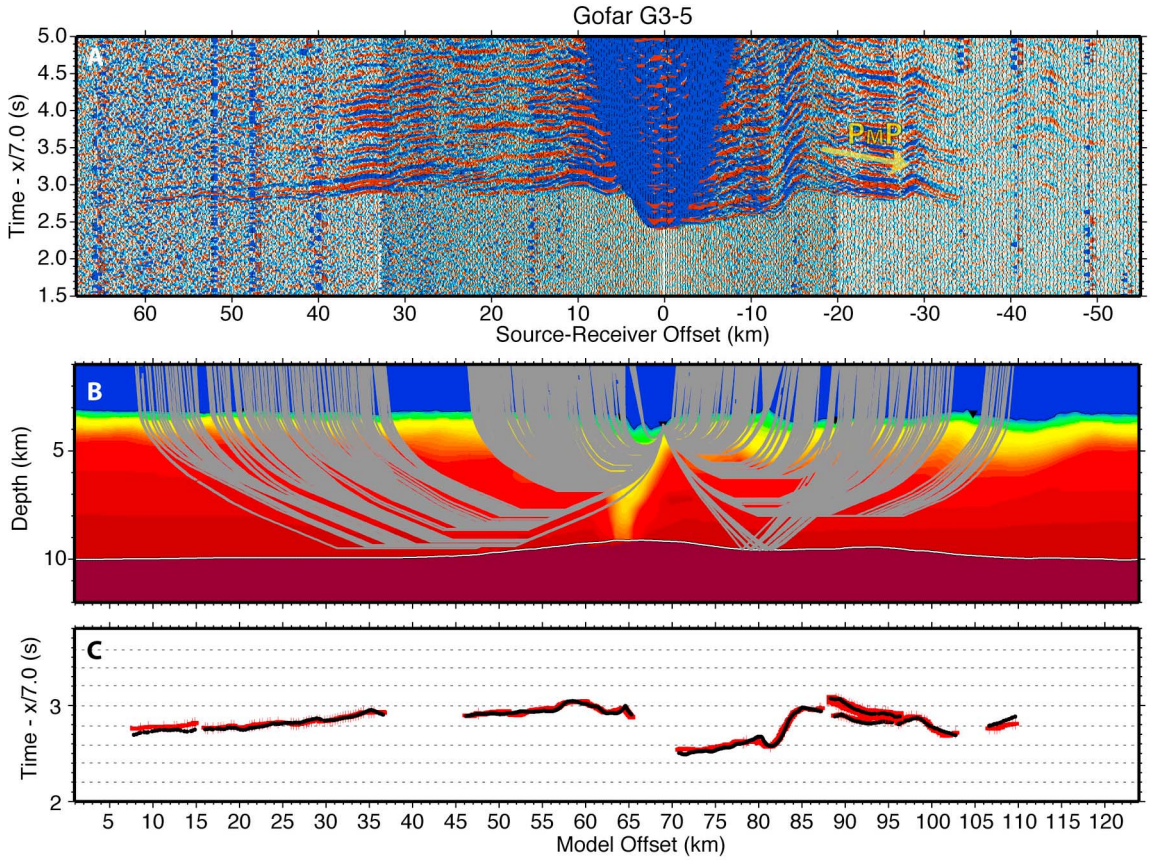

Figure 7. (a) Data, (b) ray diagram, and (c) traveltimes for station G3-5 (for more details, see Figure 5 caption). Figure 7a also has picked P_MP phases labeled above the actual arrivals. Pg phases were also picked but are not labeled here.

EPR transforms [*Wendt et al.*, 1999; *Saal and Forsyth*, 2004], as well as numerical modeling of melt generation [*Gregg et al.*, 2009], ITSCs appear to demonstrate unique geochemical compositions and dynamic melting processes. Variability in crustal thickness linked to differences in magma production at the spreading segments across the QDG area was proposed by *Pickle et al.* [2009] in a detailed analysis of regional gravity and bathymetry. The fact that we do not necessarily see an equivalent thickening in Layer 2 south of the Quebrada transform is consistent with ITSC emplacement properties varying at different offsets throughout the region. Pickle et al. observed a correlation between ITSC segment length, ridge morphology and crustal thickness that may be related to some of the variability we observe in crust created at different locations in the QDG system.

[37] A second feature of the velocity models at both the Quebrada and Gofar faults is the signature of fossil fracture zones. In Figure 16 we present the same preferred seismic velocity models displayed in terms of the velocity anomaly relative to the 1-D starting model (black lines in Figure 4). Black arrows on Figure 16 indicate the location of fracture zones crossed by the refraction lines. Low-velocity anomalies are apparent beneath the bathymetric expression of the younger fossil shear zones; however, the intensity of the velocity signature at the inactive shear zones is significantly diminished relative to the LVZ we resolve at the active faults. For example, at the location of the G2 fossil fault trace (~82 km offset on the G3 line) a very clear low-velocity anomaly is apparent within the top 2 km of the crust. The intensity and depth extent of the velocity anomaly at the fossil fault are much smaller than at the active G3 fault zone. At the location of the G1 fossil trace (~95 km offset) there is no definitive fault zone signature. If the G1 and G2 faults had a structure similar to the velocity anomaly we resolve across G3 when they were active, their current state would indicate that significant healing occurred with time as these faults became inactive and the fault zone was advected off axis. At the location of the refraction line, the G1 fault trace has had ~1.3 Myr to heal since the fracture zone accommodated opposing plate motion, and G2 has had ~0.85 Myr. Thermal contraction and thermal bending stresses would be expected at inactive oceanic fracture zones associated with cooling and differential subsidence rates of adjacent lithosphere [*Wessel and Haxby*, 1990], but these effects might be expected to enhance rather than diminish the low-velocity signature of fractured porous rocks within the shallow fossil transform domain. The evolution to higher, more typical Layer 3 seismic wave speeds at older fracture zones thus tells us something about the compressive stresses working within the lithosphere that contribute to the healing of fault-affected lower crustal rocks in a relatively short amount of time (~1 Myr). Alternatively, the G1 and G2 fracture zones may never have had a significant low-velocity

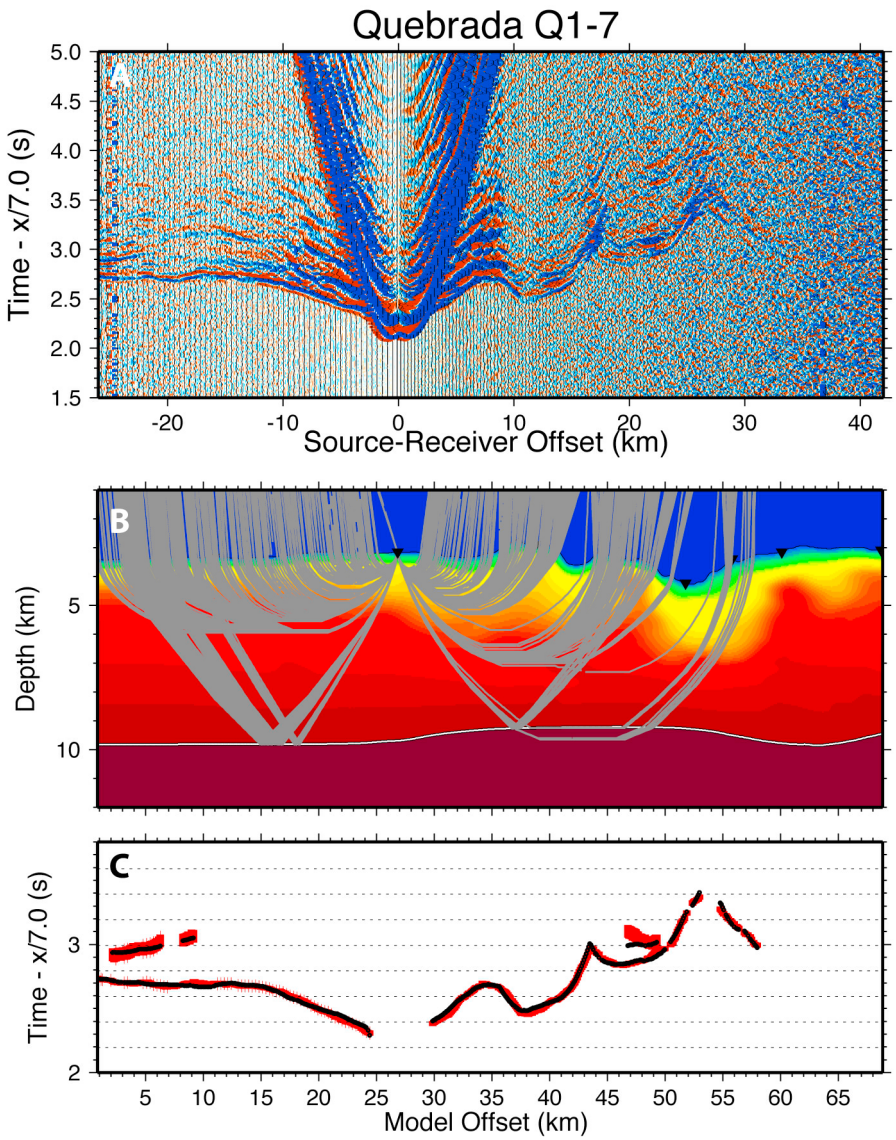

Figure 8. (a) Data recorded at Q1-7, reduced at 7.0 km/s. (b) Rays traced through preferred Quebrada Q1 velocity model using graph method. Velocity color scale is same as that shown in Figure 3. White line indicates Moho, and black triangles show receiver locations. (c) First-arrival traveltime picks for Q1-7 (red) compared to the modeled traveltimes using preferred P wave velocity model (black). Heights of modeled data points indicate the assumed traveltime pick error.

zone in the midcrust to lower crust, as appears to be the case at the Clipperton fault located at 10°N on the EPR [*Van Avendonk et al.*, 1998, 2001].

[38] Lateral velocity heterogeneity is also apparent on the Q1 line throughout the entire Quebrada transform domain, ~30 km south of the active fault segment (Figure 16). Although the poor lower crust resolution at Q1 makes the relative difference in the active and fossil shear zone signatures less certain, the diminished shallow low-velocity signature that coincides with the Q2–Q4 fault traces seems to be consistent with evidence of past faulting and lithospheric healing that we observe at Gofar. The continuity of the low-velocity zone within the upper crust throughout the entire Quebrada fault domain to the south of Q1 also raises the question of whether some degree of distributed shear may occur across the wide Quebrada fault zone valley, particularly within the shallowest crustal layers.

6.2. Interpretation of Low-Velocity Fault Zone

[39] In order to identify material properties that influence earthquake behavior at oceanic transforms it is necessary first to consider what type of material variation may be causing the significantly reduced seismic velocities (0.5–1.0 km/s, 10–20%) we image at both fault zones. Typical oceanic crustal Layer 3 extends from 2 to 3 km beneath the seafloor to the base of the crust. This plutonic layer tends to exhibit only a modest increase in velocity with depth due to temperature, variation in gabbroic composition, and closure of microfractures with increasing effective pressure [*Iturrino et al.*, 1991, 1996; *Carlson and Miller*, 2004]. We are most interested in interpreting the fault zone velocities within

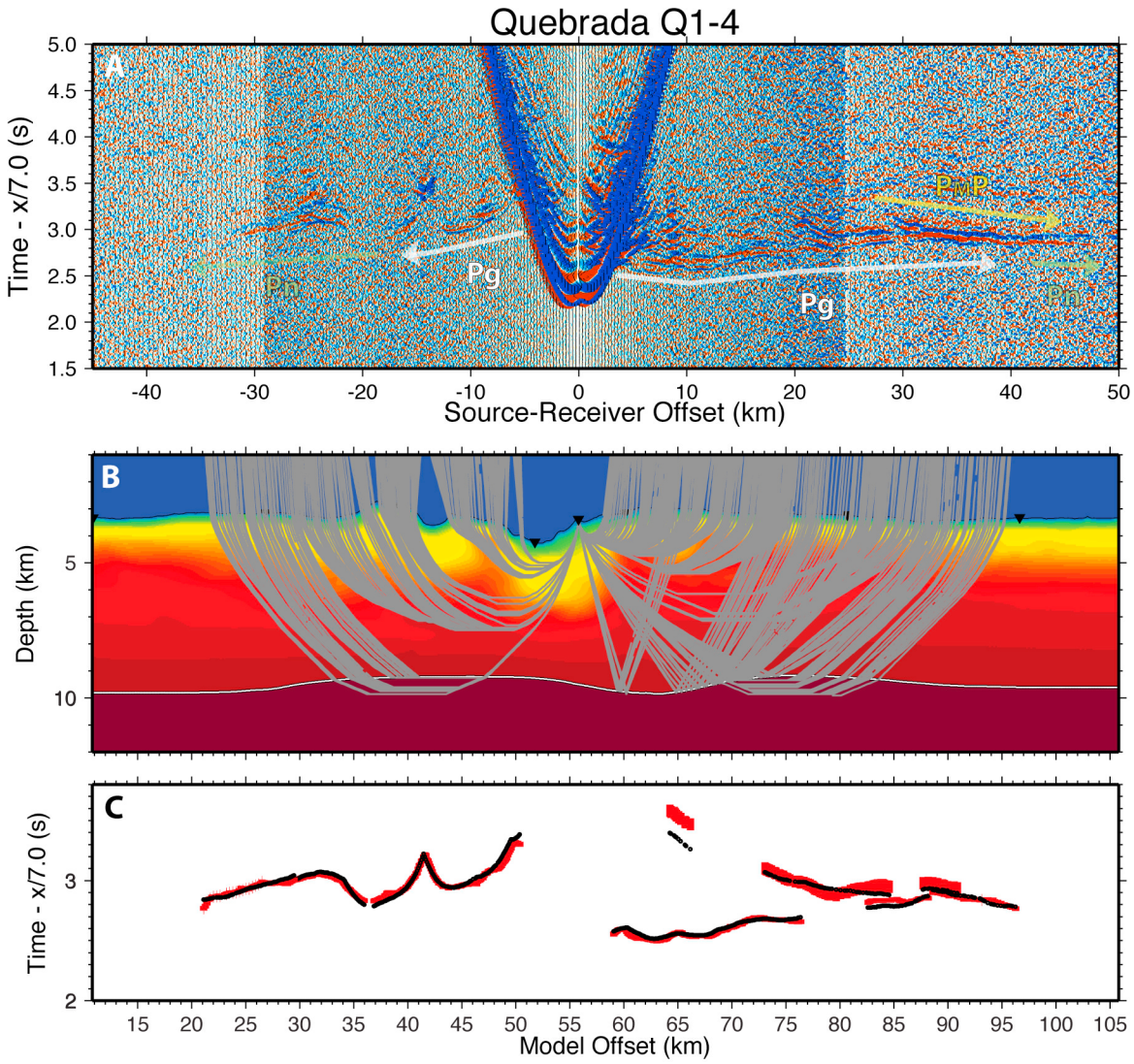

Figure 9. (a) Data, (b) ray diagram, and (c) traveltimes for station Q1-4 (for more details, see Figure 8 caption). Figure 9a also has picked phases labeled below (Pg, Pn) and above (P_MP) the actual arrivals so as not to obscure the data.

Layer 3, as this likely corresponds to the seismogenic zone at the relatively warm Pacific transforms, and thus may provide information about frictional heterogeneity that affects earthquake behavior. Based on previous studies of continental and oceanic strike-slip fault zones, the two most likely candidates for the significant reduction in seismic velocities we image within the central transform zone are intense fracturing associated with shear strain [*Tréhu and Purdy*, 1984; *Chester et al.*, 1993; *Eberhart-Phillips et al.*, 1995; *Thurber et al.*, 1997; *Van Avendonk et al.*, 1998; *Schulz and Evans*, 2000; *Van Avendonk et al.*, 2001; *Cochran et al.*, 2009] and mineral alteration [*Bonatti*, 1978; *Calvert and Potts*, 1985; *Cannat et al.*, 1990; *Detrick and Purdy*, 1980; *Detrick et al.*, 1982; *Minshull et al.*, 1991; *White et al.*, 1984; *Detrick et al.*, 1993; *Faulkner et al.*, 2003]. It is likely that both of these processes are at work to some degree within the transform domain. By evaluating the details of how seismic velocity is affected by increases in porosity and/or alteration, we gain some insight into which of these processes is the dominant cause of the velocity reduction observed in our tomography results.

[40] The degree of fracturing and resulting porosity required to explain the low velocities we observe is highly dependent on the geometry assumed for fluid-filled pores. In Figure 17a, we show the Hashin-Shtrikman (HS) bounds on the compressional wave seismic velocity for seawater-saturated gabbro over a range of porosities. The upper and lower HS bounds encompass the full range of possible pore geometries [*Hashin and Shtrikman*, 1963; *Avseth et al.*, 2005]. This calculation leads to a very wide range of seismic velocities that are possible for a given porosity, thus making it advantageous to consider likely fracture geometries associated with the damage zone surrounding the fault. Several field studies of continental strike-slip faults have identified fractures in the damage zone that are crack-like, with large aspect ratios that are variably oriented with respect to the fault plane [*Chester et al.*, 1993; *Savage and Brodsky*, 2011]. Based on theoretical calculations of scattering phenomena [*Kuster*

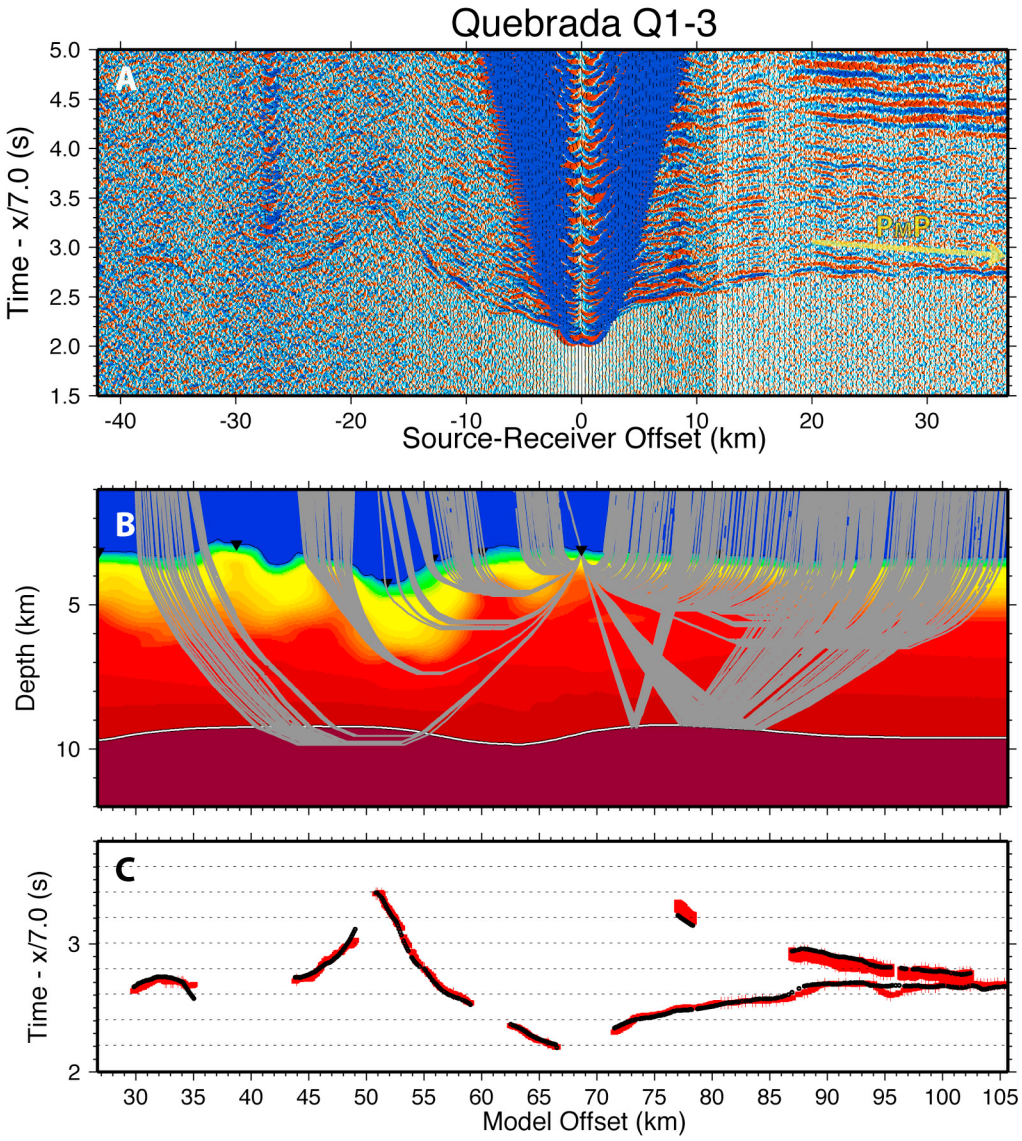

Figure 10. (a) Data, (b) ray diagram, and (c) traveltimes for station Q1-3 (for more details, see Figure 8 caption). Figure 10a also has picked P_MP phases labeled above the actual arrivals. Pg and Pn phases were also picked but are not labeled here.

and Toksöz, 1974], the crack aspect ratio (α) can be taken into account as well as the concentration of pores and elastic moduli of the constituent phases to estimate seismic velocity. Porosity associated with crack-like pores has a greater effect on the elastic properties compared to spherical pores, and assuming aspect ratios of oblate spheroidal pores that range from 10 to 1000, the slowest crustal seismic velocities we determine within the seismogenic zone at the Gofar fault (>∼3 km beneath the seafloor [*McGuire et al.*, 2012]) are consistent with a range of porosity values from roughly 1.5 to 8% depending on pore geometry (Figure 17c). As some amount of lateral smoothing has likely occurred in the tomographic inversion process, the real fault zone rocks may exhibit even slower seismic velocities within a narrower zone, making these values a lower bound on the range of possible porosity.

[41] Metamorphic alteration can also lead to significantly reduced seismic velocities in rocks of mafic composition. If fluid pathways exist down to lower crust and upper mantle depths, alteration of clinopyroxene and olivine in gabbroic rocks to amphibole, serpentine and talc, and serpentinization of upper mantle peridotite is likely to occur within the fault zone. Serpentinites have been dredged along Atlantic fracture zones [*Bonatti*, 1976, 1978] as well as at a few transform faults in the Pacific [*Anderson and Nishimori*, 1979; *Hébert et al.*, 1983; *Cannat et al.*, 1990; *Hekinian et al.*, 1992], and serpentine diapirism has been proposed as the primary cause of transverse ridge formation at Atlantic transform faults [*Bonatti*, 1978]. The anomalously low strength of serpentine and reduced density relative to lower crustal rocks is thought to mobilize altered ultramafic rocks, enabling them to intrude shallower crustal depths. In support of this, seismic refraction experiments across Atlantic fracture zones have imaged low-velocity zones accompanied by reduced crustal thickness, which are interpreted as resulting from upper mantle alteration and uplift [*Detrick and Purdy*, 1980; *Detrick*

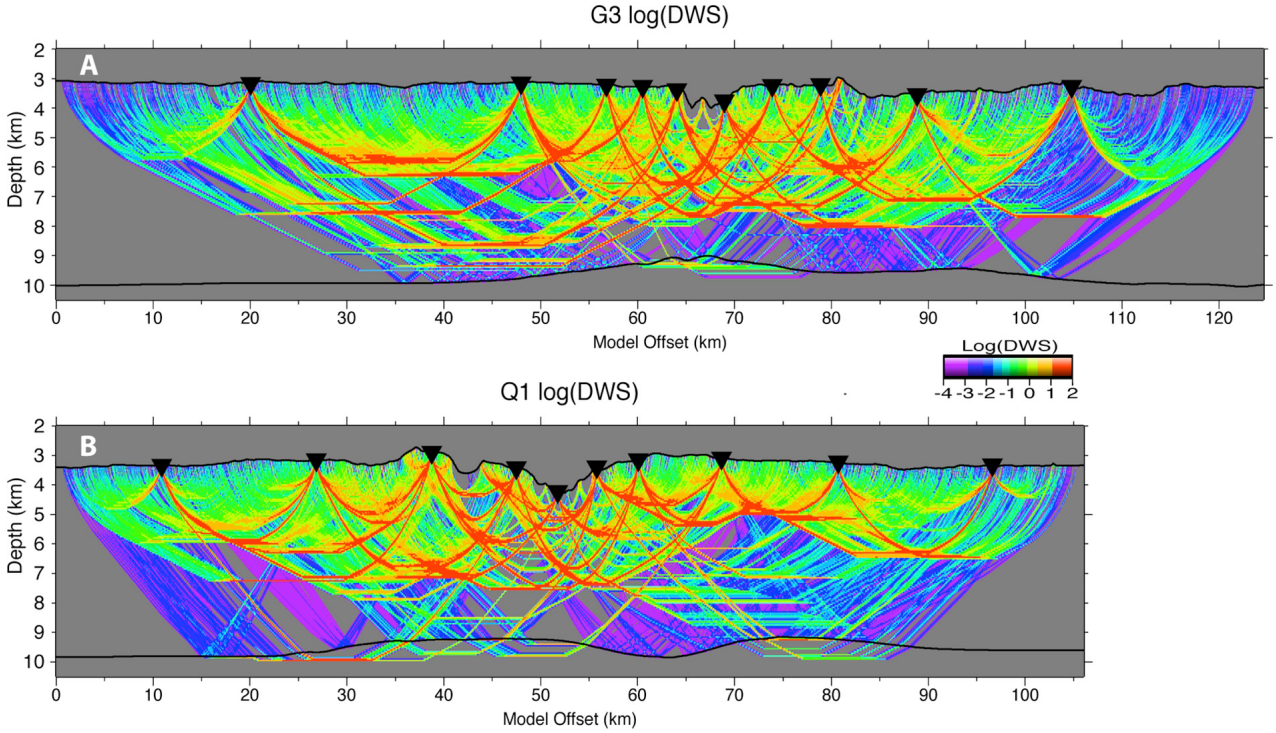

Figure 11. The derivative weight sum (DWS) for (a) the G3 and (b) Q1 models. The DWS is a weighted sum of the elements of each column of the Fréchet matrix [*Van Avendonk et al.*, 1998] and is a nondimensional value that indicates the ray density throughout the model.

et al., 1982; *White et al.*, 1984; *Minshull et al.*, 1991; *Detrick et al.*, 1993]. Serpentine and talc also outcrop along the Parkfield section of the San Andreas fault, and their presence has been proposed as one possible explanation for the primarily aseismic nature of the fault segment, due to their low strength relative to other crustal crystalline and sedimentary rocks [*Moore et al.*, 1997].

[42] Although we do not see significant thinning of the crust within the Gofar and Quebrada transform domains, fault zone velocities are consistent with elastic properties of partially serpentinized mantle rocks. In Figure 17a, HS bounds for the range of seismic velocities associated with different degrees of lower crust and upper mantle alteration are displayed as gray envelopes. Due to the unique elastic properties of serpentine and the high olivine content of peridotite, alteration of mantle phases have a much larger influence on seismic velocity than alteration of gabbro that would be expected in the lower crust. Using the HS mixture relation and assuming that amphibole is the primary alteration phase in lower crust gabbroic rocks, metamorphism of clinopyroxene alone cannot have a large enough effect on the elastic properties to explain the reduction in seismic velocities we determine within the fault zone (Figure 17a). If we assume, rather, that altered peridotite is present at crustal depths within the central fault zone at Gofar, mantle material that is 50–90% percent altered would exhibit elastic properties consistent with the slowest crustal seismic velocities we determine within the seismogenic zone (Figure 17c). Similarly, olivine-rich lower crust rocks, analogous to troctolites found along slow spreading ridges [*Miller and Christensen*, 1997; *Dick et al.*, 2008], could also reduce seismic velocities at the base of the crust at Gofar if they were serpentinized >70% (Figure 17c). These rocks are not commonly found on the EPR, but they could be present in the QDG region, where intratransform crustal emplacement processes are likely to be different from more typical EPR segments. If they are present at Gofar, the influence of serpentinized troctolites on fault zone mechanics would be similar to that of altered peridotite.

[43] The question of whether or not serpentine is present within the fault zone at Gofar or Quebrada has implications for the frictional properties that control earthquake behavior. Because the density of partially serpentinized peridotite or olivine-rich crustal rock is significantly reduced relative to unaltered mafic rocks (Figure 17c), gravity observations should provide some evidence for the presence of a low-density body of serpentinized mantle if one is present within the fault zone. In Figure 18, we display the free-air anomaly (FAA) measured over the QDG faults [*Pickle et al.*, 2009], as well as gravity anomaly profiles parallel to the seismic refraction lines. Variations in FAA reflect the shallow density structure; low FAA is associated with bathymetric lows, zones of thicker crust, hotter upper mantle, and/or less dense crustal material. Although interpreting gravity data, like seismic velocity, is nonunique, by making some simple assumptions about the density structure of the crust, we can compare the measured gravity anomaly to that expected if serpentinized mantle material has been emplaced in the crust within the Gofar and Quebrada fault zones (Figure 19, solid red lines). Based on this analysis, we find that along the "normal" EPR crust (south of Gofar or north of Quebrada), variations in the amplitude of the observed FAA are

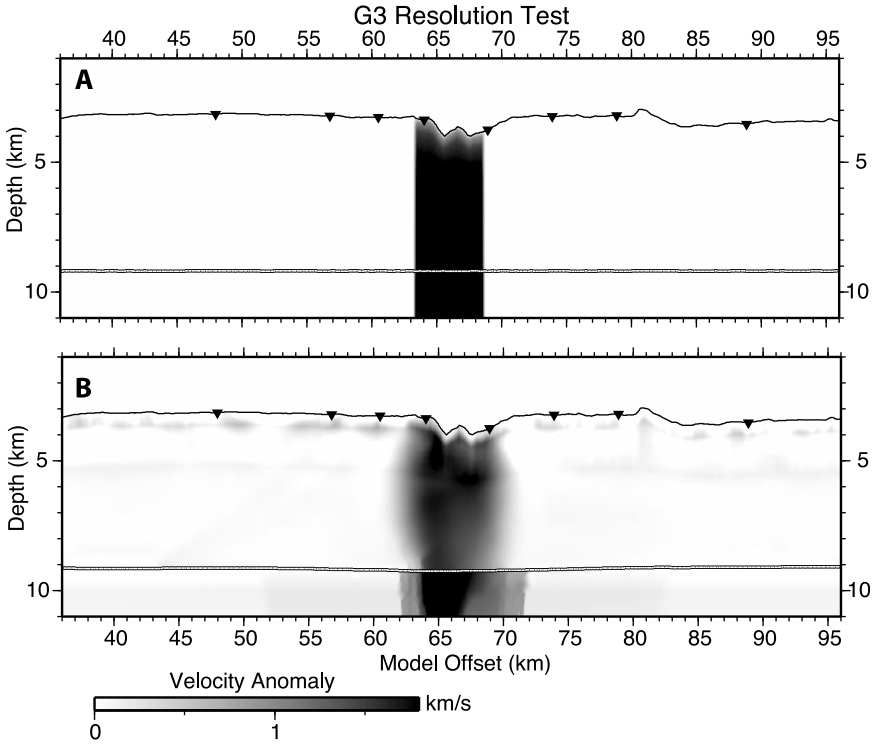

Figure 12. (a) Resolution test for a 5 km wide fault zone with P wave velocities reduced by 30% that extends throughout the crust and upper mantle. Synthetic data were first calculated by forward modeling traveltimes with the same source-receiver geometry used in the tomographic inversion for the Gofar G3 velocity model and the fault zone anomaly shown in Figure 12a. Synthetic traveltimes were then modeled using the tomographic strategy outlined in section 3.2. (b) With the exception of some smoothing in the lower crust, the 5 km wide fault zone signal is reproduced well with the model resolution available here.

consistent with variability due to bathymetric relief. Within the intratransform region (north of Gofar and south of Quebrada), there is an offset between the observed and modeled gravity signal. This offset indicates that there are differences between the normal EPR lithosphere and that formed within the intratransform region, and that these differences are not resolved in the tomography results and thus not incorporated into the density model. A shallower Moho or a cooler upper mantle, perhaps due to distinct crustal accretion or mantle flow processes, could explain the increased gravity anomaly within the intratransform region. However, this regional variability has very little impact on the gravity signal above the transform faults. The observed gravity anomalies above the fault zones are moderate gravity lows. Based on the simple models, these lows can be explained almost entirely by bathymetric relief alone; no density reduction within the crust at the transforms is needed to match the observed gravity (Figure 19, dashed red line). Moreover, the density variation expected for a fault zone composed of serpentinized mantle material (for Gofar we assume 40% alteration over a zone at least 2 km wide) predicts a free-air anomaly low that is much larger than what is observed. Thus, the moderate amplitude of the gravity anomalies above the transform faults provides no evidence for large, low-density bodies within the fault zones. Instead, the gravity models suggest that the mechanism reducing seismic velocity in the fault zones is one that leaves density mostly unchanged. Variation in porosity provides such a mechanism. An increase in porosity of less than 10% is enough to account for the imaged low velocities, and the density contrast due to a porosity change of this magnitude would produce a gravity signature that is below the measurement sensitivity. The gravity data thus tend to favor enhanced porosity over bulk mineral alteration as the primary mechanism for seismic velocity reduction within the fault zones.

[44] The crustal velocity signatures of fossil fracture zones to the north and south of Gofar and Quebrada, respectively, provide additional evidence in favor of the presence of enhanced porosity rather than a serpentinized fault zone. The G3 and Q1 transects cross several previously active fracture zones associated with the G1–2, and Q2–4 segments. The low-velocity signature we resolve across these fracture zones is relatively much diminished or altogether absent compared to the primary active fault LVZ. This indicates that either the velocity structure at the other fault segments is fundamentally different from those at G3 and Q1, or an aging process has altered the material within the fossil fracture zones, restoring the elastic properties to more closely resemble typical Layer 3 velocities. The evolution of high-porosity oceanic crustal material from slower to faster seismic velocities with age has been documented previously in the shallow crust [*Houtz and Ewing*, 1976; *Purdy*, 1987]. Because young oceanic lithosphere is in a state of compression, especially at lower crustal depths where the confining pressure is high (equal to σ_1, the maximum compressive stress in this environment), crack closure in fractured oceanic crust,

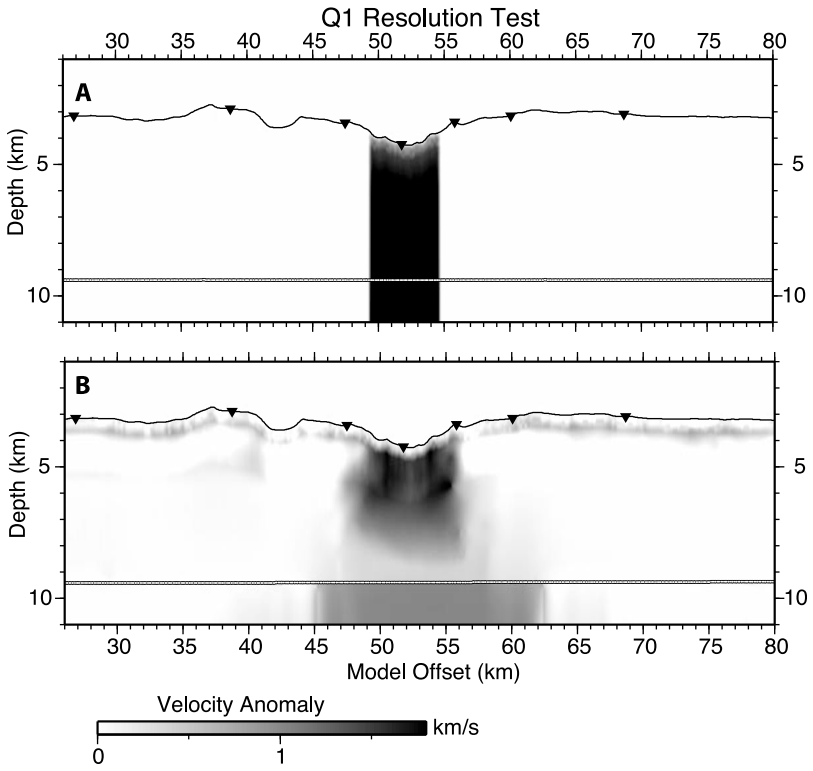

Figure 13. Resolution test similar to that presented in Figure 12, here for the model and data configuration from the Quebrada Q1 tomographic inversion. (a) Model configuration used to produce the synthetic data set. (b) The 30% velocity reduction within a 5 km wide zone is resolved throughout the upper crust; however with ray coverage available for the Q1 data set, the velocity anomaly is not well resolved in the lower crust or upper mantle.

modifications to the geometry of cracks, or infiltration by precipitation of hydrothermally derived material could lead to a change in the elastic properties as the fracture zone becomes inactive and material is advected off axis. Alternatively, if the LVZ anomaly were a result of serpentinized mantle material, there is little reason to believe that seismic velocities would be restored with time. Rather, the degree of hydrothermal alteration would be expected to increase as the lithosphere ages and cools, and the volume of the crust within the serpentine stability field increases [*Roland et al.*, 2010].

[45] Ultimately, if enhanced fluid-filled porosity occurs at depth within the fault zone, some alteration will also occur, and if hydrated phases are present in the lower crust, some connected fluid pathways, and likewise, some degree of enhanced porosity must also be present. Based on the results of our effective media analyses coupled with observations of the gravity anomaly and fossil fracture zones, it appears that the extensive damage zones we image at the Gofar and Quebrada faults are associated with enhanced porosity throughout the crust, probably accompanied by some moderate degree of crustal alteration.

6.3. Relationship Between Fault Zone Structure and Seismic Coupling

[46] The primary objective of this experiment was to characterize the macroscale material properties of the Gofar and Quebrada faults and to relate these properties to their mechanical behaviors, specifically the ability of these faults to generate large earthquakes. In this regard, the mechanical behaviors of these two faults differ. The Gofar fault releases ~50% of its plate motion in large earthquakes, routinely generating M ~ 6 earthquakes, while the Quebrada fault accommodates almost all of its plate motion without generating large earthquakes [*McGuire*, 2008]. Directly relating the macroscopic seismic coupling properties to the imaged velocity structure of these two faults is not straightforward however, based on recent observations that earthquake generation behavior on Gofar varies substantially along strike. While we intended the Gofar refraction line to cross through a portion of the fault that repeatedly ruptures in M 6 earthquakes, seismic recordings from the yearlong OBS deployment revealed that the line actually crossed through a long-lived barrier to seismic rupture propagation, which lies between two fault patches that repeatedly rupture in M 6 earthquakes [*McGuire et al.*, 2012]. Figure 20a shows the locations of the foreshocks and aftershocks of the 18 September 2008 M_w 6.0 Gofar earthquake and the location of the G3 seismic refraction transect. The refraction line crosses through the foreshock zone, which failed in a swarm of >20,000 microearthquakes (M < 4) in the week before the M_w 6.0 main shock ruptured the segment to the west (denoted by the aftershocks in Figure 20). As discussed by *McGuire et al.* [2012], the week-long foreshock sequence was likely triggered by a large, aseismic creep event. Thus, our G3 model may actually represent the best constrained image of an EPR transform fault zone that is incapable of generating large earthquakes and fails primarily aseismically.

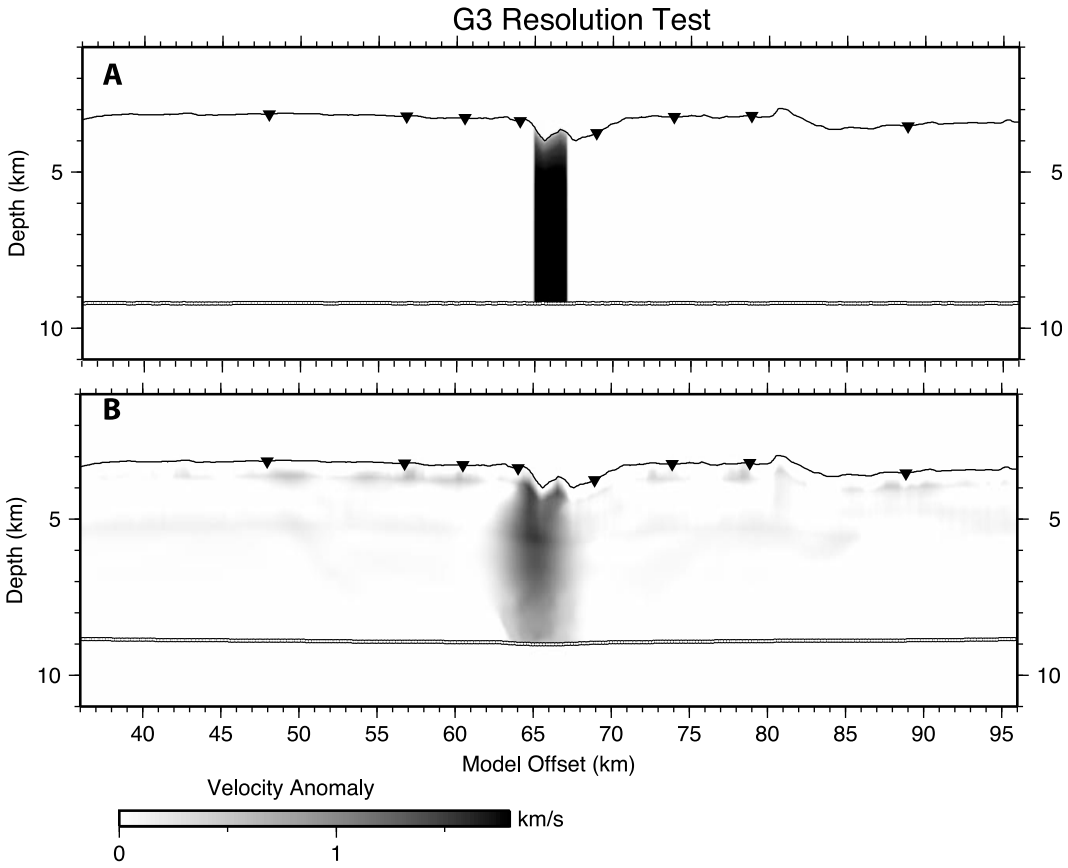

Figure 14. (a) Resolution test for a 2 km wide fault zone with P wave velocities reduced by 30% that extends throughout the crust on the G3 line. (b) A 2 km wide fault zone signal is reproduced well with the model resolution available here, though the amplitude of the low-velocity anomaly is reduced in the lower crust and the signal is smeared somewhat at midcrustal depths.

[47] The best images of an EPR transform fault zone that *is* capable of rupturing in large (M 6+) earthquakes are from the *Van Avendonk et al.* [1998, 2001] studies of the Clipperton transform fault. This fault periodically sustains M ~ 6.6 earthquakes that likely rupture the entire fault segment. In fact, Clipperton is the most efficient RTF in terms of generating large earthquakes relative to its thermally estimated seismogenic area [*Boettcher and Jordan*, 2004]. Based on the velocity structure determined by *Van Avendonk et al.* [1998, 2001], the Clipperton fault does not show a significant low-velocity zone at seismogenic depths in the region that generates M 6.6 ruptures. P wave velocities in the midcrust to lower crust within the active fault zone are >6 km/s, indicating relatively intact gabbro [*Van Avendonk et al.*, 1998, Plate 1]. The Clipperton model of Van Avendonk et al. provides a stark contrast to our G3 model where P wave velocities of <~5.5 km/s are clearly resolved in the seismogenic zone (midcrust to lower crust). The difference between the seismic velocity structures at the Clipperton fault as compared to the Gofar fault is also made apparent by simply comparing the arrival times of crustal refracted waves that pass through the lower crust across the fault zone. Pg phases passing >4 km beneath the seafloor within the fault zone show relative delay times of <0.2 s at Clipperton as compared to 0.4 s at Gofar. These differences suggest that the RTF segments that generate large earthquakes have relatively intact gabbro in the seismogenic zone while segments that fail aseismically and serve as long-lived rupture barriers are composed of highly fractured ≥2 km wide damage zones that extend through the crust all the way to the Moho (Figure 3).

[48] We would like to understand the mechanistic connection between high porosity at seismogenic depths within the Gofar foreshock zone and this zone's persistence as a rupture barrier. Any such understanding should include an explanation of the observed structural and seismic properties of this section of the fault, and so we summarize those here. The area sampled by the G3 refraction transect has been a barrier to large seismic rupture throughout the past 4 seismic cycles [*McGuire*, 2008]. We thus refer to this region of the fault as the rupture barrier zone. The rupture barrier zone apparently has high porosity relative to the surrounding crust and to other nonbarrier RTFs, and it does not appear to be composed of a massive body of hydrothermally altered crust or mantle material. Additionally, based on OBS recordings during the 2008 QDG experiment, the depth extent of microseismicity in the rupture barrier zone (~2–9 km; primarily foreshocks) is greater than the depth of seismicity within the main shock/aftershock section of the fault (~2–6 km) immediately to the west (Figure 20) [*McGuire et al.*, 2012]. A mechanism that relates enhanced porosity to rupture

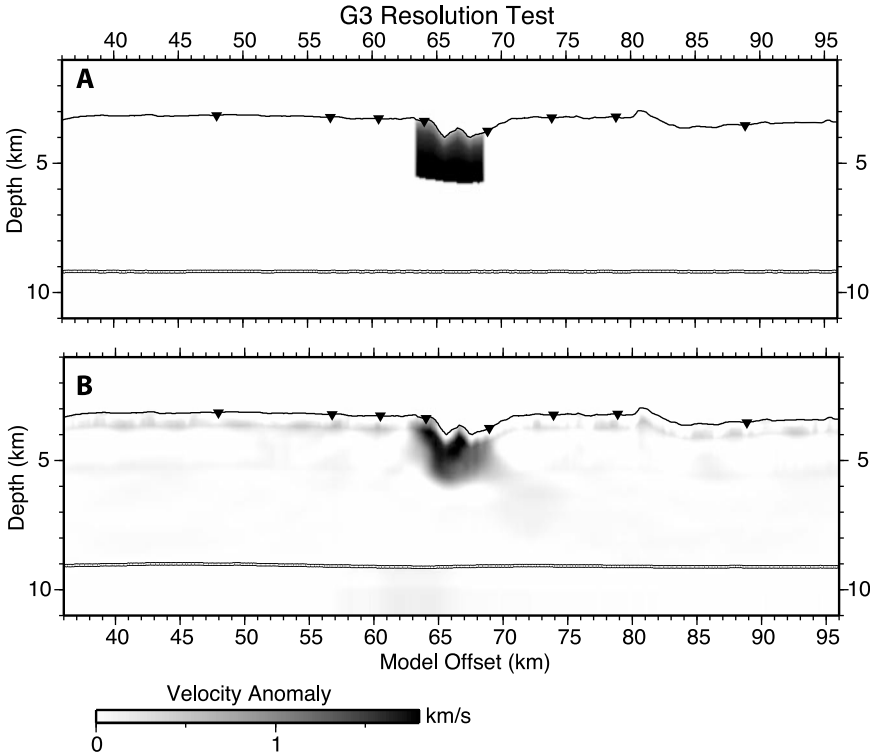

Figure 15. (a) Resolution test for a 5 km wide, 30% reduced P wave velocity fault zone that is confined to the shallowest 2 km of the upper crust. (b) Using the model and data geometry available for the G3 line, the shallow velocity anomaly is well resolved, with little or no smearing of the signal laterally or in depth.

barrier behavior should thus include or, at a minimum, allow a consistent explanation of each of the known properties of this segment.

[49] Variation in the depth extent of seismicity along strike at Gofar, and the inferred high porosity within the rupture barrier zone suggest that fluids and fluid flow play an important role in determining the physical conditions within this region. Specifically, the enhanced depth of microseismicity indicates that the thermal structure should be generally cooler here. In Figure 20, we display the thermal structure calculated for the G3 fault using a model similar to that developed by *Roland et al.* [2010]. This model, which includes hydrothermal cooling decreasing downward to a maximum depth of 6 km (Nusselt number, $Nu = 6$) along the entire length of the Gofar fault, shows the temperature at the base of the aftershock zone to be very close to the expected frictional stability transition (~500–600°C) [*Boettcher et al.*, 2007; *He et al.*, 2007]. Since foreshock seismicity within the rupture barrier zone appears to be significantly deeper than this predicted stability transition, some mechanism of enhanced cooling is required to explain the depth extent of seismicity. One possibility is that additional advective heat transport associated with local, more robust fluid circulation [*McGuire et al.*, 2012] is facilitated by a moderate amount of transtension in the vicinity of the rupture barrier zone. A very mild change in strike (~3°) of the Gofar G3 fault segment, apparent in the bathymetric expression of the fault trace near the rupture barrier, is roughly consistent with this hypothesis. Deep fluid circulation is also consistent with the apparent increase in porosity at seismogenic depths, as interpreted from the lower crust velocity structure within the G3 rupture barrier.

[50] Enhanced fluid-filled porosity and fluid circulation offer an explanation for the overall velocity-strengthening nature of the rupture barrier zone associated with one or both of two possible processes: (1) porosity and trapped fluids at great depths lead to heterogeneous stress conditions and (2) metamorphic alteration lubricates the fault zone with weak minerals. While these may occur contemporaneously where fluids are present within the lower crust and upper mantle at Gofar, either mechanism could potentially account for the rupture barrier nature of the fault zone surrounding the G3 refraction transect.

[51] Within a fault environment where fluids are distributed over a wide, variably fractured area, localized zones of elevated or reduced pore fluid pressure would produce strong heterogeneity in stress conditions. Dilatancy strengthening, related to the tendency for pore space to increase and pore fluid flow to be restricted under shear, may act to suppress dynamic slip, even within otherwise velocity weakening frictional conditions [*Segall and Rice*, 1995; *Liu and Rubin*, 2010; *Segall et al.*, 2010]. Based on numerical simulations and observations in the laboratory, it also seems that the effect of dilatancy increases within wider shear zones [*Segall and Bradley*, 2012], consistent with the highly fractured, low-velocity structure we infer at Gofar. Assuming this dilatancy strengthening mechanism, seismic rupture that initiates on segments to the east or west of the rupture barrier

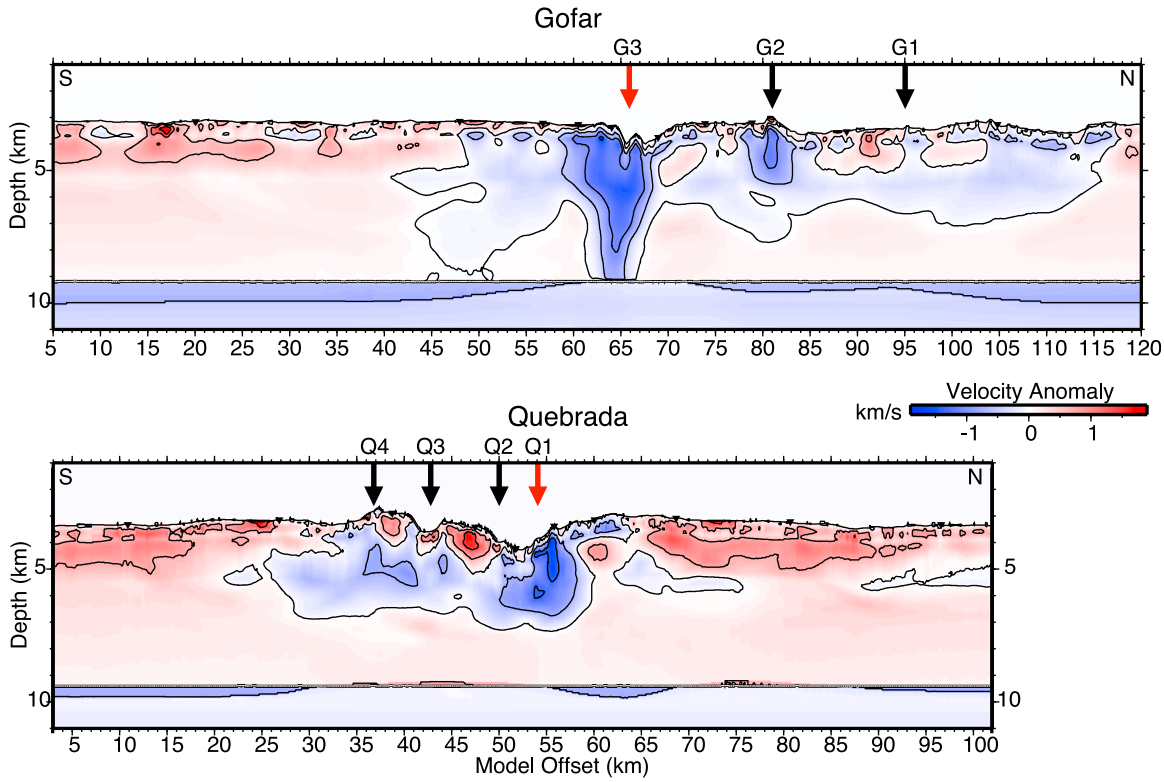

Figure 16. Preferred velocity models determined for the Gofar G3 line and Quebrada Q1 line (displayed in Figure 3), plotted in terms of the velocity anomaly relative to the starting model (shown in Figure 4c) contoured (black lines) every 0.5 km/s. Red arrows show the location of the active fault traces; black arrows show the locations where the transects cross fossil fracture zones associated with faults (top) G2 (∼0.88 Myr since active) and G1 (∼1.29 Myr since active) to the north of G3 and (bottom) Q2–Q4 (<1.1 Myr since active) to the south of Q1.

region would terminate where fault zone structure transitions from intact, relatively undisturbed gabbro, to highly fractured fluid-filled porous material. Inline with our imaged low velocities along the G3 transect, infiltration of fluids to great depths could cool the lithosphere and depress the frictional stability transition, enabling deep microseismicity, while also promoting potentially widespread stabilizing interactions between pore fluids and slip.

[52] Hydrothermally altered minerals are likely to be present along RTFs that have been infiltrated with water, and these minerals can also affect the seismogenic properties of the fault zone. Numerical models indicate that pressure and temperature conditions within the lower crust and upper mantle are favorable for alteration of olivine to serpentine and/or talc where water is present at these depths [*Roland et al.*, 2010]. Altered lower crust and upper mantle rocks including serpentine and talc, are commonly dredged at transform faults [*Tucholke and Lin*, 1994], including at least one example from a fast spreading transform on the EPR, the Garrett transform, just a few hundred kilometers south of the QDG system [*Cannat et al.*, 1990; *Hekinian et al.*, 1992]. Given the enhanced porosity throughout the crust, it is likely that at a minimum, some serpentinization has occurred in isolated regions that could be unresolvable by gravity and refraction techniques. Laboratory studies have shown that under certain stress and temperature conditions, serpentine minerals demonstrate velocity-strengthening behavior that would inhibit unstable earthquake nucleation [*Moore et al.*, 1997; *Reinen*, 2000; *Moore and Lockner*, 2007]. It is thus possible that even a very narrow zone of serpentine at seismogenic depths could promote stable sliding within an inner fault core, resulting in the rupture barrier behavior.

[53] The presence of enhanced fluid circulation in the rupture barrier zone is consistent with our interpretation of a wide zone of highly fractured porous material based on the LVZs we image across the Gofar and Quebrada faults. In particular, the considerable thickness and depth extent of the region of reduced seismic velocities and increased fracturing at G3 would likely facilitate deep fluid penetration, and via dilatancy strengthening and/or the presence of velocity-strengthening altered phases, provide a mechanism for the unique mechanical behavior observed on the Gofar fault. Based on our results, it seems likely that other poorly coupled RTFs in the Pacific may contain similar regions of highly damaged, porous fault zone structure, which limit the amount of slip that can occur as unstable shear localization along narrow, highly competent slip zones during large earthquakes. Our velocity profiles and seismicity observations suggest that the presence of thick zones of fractured, fluid-saturated material on RTF systems promote important along-strike variation in slip behavior and help to explain the overall low seismic coupling that has been inferred at oceanic

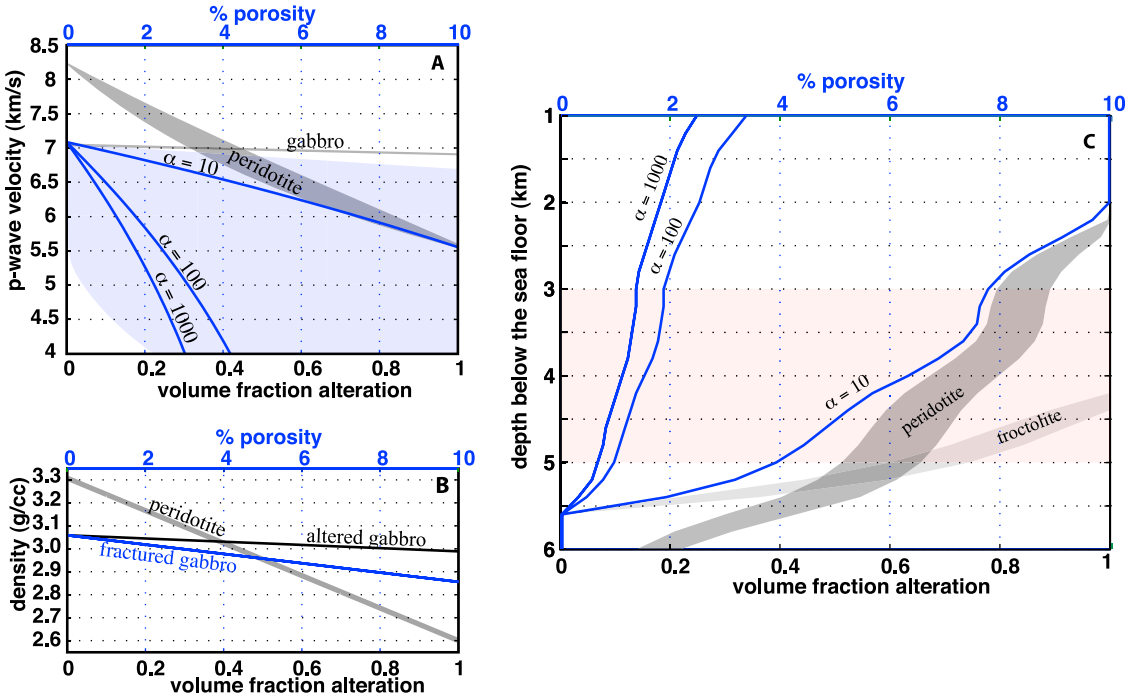

Figure 17. Effective media analyses assuming fluid-saturated porosity (blue curves throughout) or alteration of upper mantle material (black/gray curves). (a) Seismic P wave velocity variation with increased seawater-saturated porosity in gabbro (top axis) or alteration of upper mantle peridotite (bottom axis) using Hashin-Shtrikman (HS) mixing relations [*Hashin and Shtrikman*, 1963] and the two-phase media relations of *Kuster and Toksöz* [1974] for cracks with aspect ratios (α) of 10, 100, and 1000. Gabbro composition used here is 18% olivine, 47% plagioclase, and 35% clinopyroxene. Elastic properties come from *Carlson and Miller* [2004] and are corrected for depth. Peridotite composition is 90% olivine, 4% pyroxene, and 6% hornblende, which we take along with the elastic properties from *Iturrino et al.* [1996]. HS bounds are calculated assuming a depth of 4 km below the seafloor. Velocities are also corrected for the effect of closing microfractures with depth. (b) Change in bulk density associated with increased porosity (top axis) and alteration of peridotite (bottom), equivalent to material properties shown in Figure 17a. (c) The predicted porosity (top axis) or percent alteration (bottom axis) based on the seismic velocities determined for the Gofar fault zone (slowest velocities sampled from G3 model, ~65 km offset). Porosity and degree of alteration are calculated assuming the HS upper and lower velocity bounds for peridotite and the Kuster and Toksöz two-phase media relations for porosity values, as shown in Figure 17a. Troctolite trend shows the degree of serpentinization required to match our seismic velocity model for olivine-rich crustal rocks (troctolite composition 30% olivine, 69% plagioclase, and 1% clinopyroxene from *Miller and Christensen* [1997]). Light red shaded region shows the depth range of the Gofar seismogenic zone within the crust used to estimate values for porosity and degree of alteration reported in the text. This depth range is based on seismicity observations presented in Figure 20.

transform faults globally [*Bird et al.*, 2002; *Boettcher and Jordan*, 2004].

7. Conclusions

[54] Seismic tomography results presented here show a significant low-velocity zone associated with the active fault trace at two distinct oceanic transforms on the equatorial EPR. These LVZs are greater than 5 km wide in the shallow crust, and where our velocity models are well resolved at the Gofar fault, as wide as ~2 km at the base of the crust. This variation in elastic properties within the seismogenic zone at Gofar is likely indicative of important material variation that may influence seismic behavior. Based on effective media analyses, we determine that the seismic velocities imaged within the seismogenic zone (>3 km depth) of the Gofar fault are consistent with increased porosity in gabbro of 1.5–8% in the form of fluid-filled, high aspect ratio pores (α = 10–100). The slowest seismic velocities within the seismogenic zone are also consistent with the presence of mantle peridotite that has been 50–90% altered, although free-air anomaly gravity observations and evidence for "healing" of the velocity anomaly at fossil fracture zones do not support the presence of serpentine or talc in high quantities within the fault zone. However, it is likely that if increased porosity is responsible for the wide LVZs we image, some degree of alteration has also occurred in the lower crust and upper mantle. Based on observations of fault rupture properties from a yearlong deployment of a 40 element OBS array in 2008, fault structure at the G3

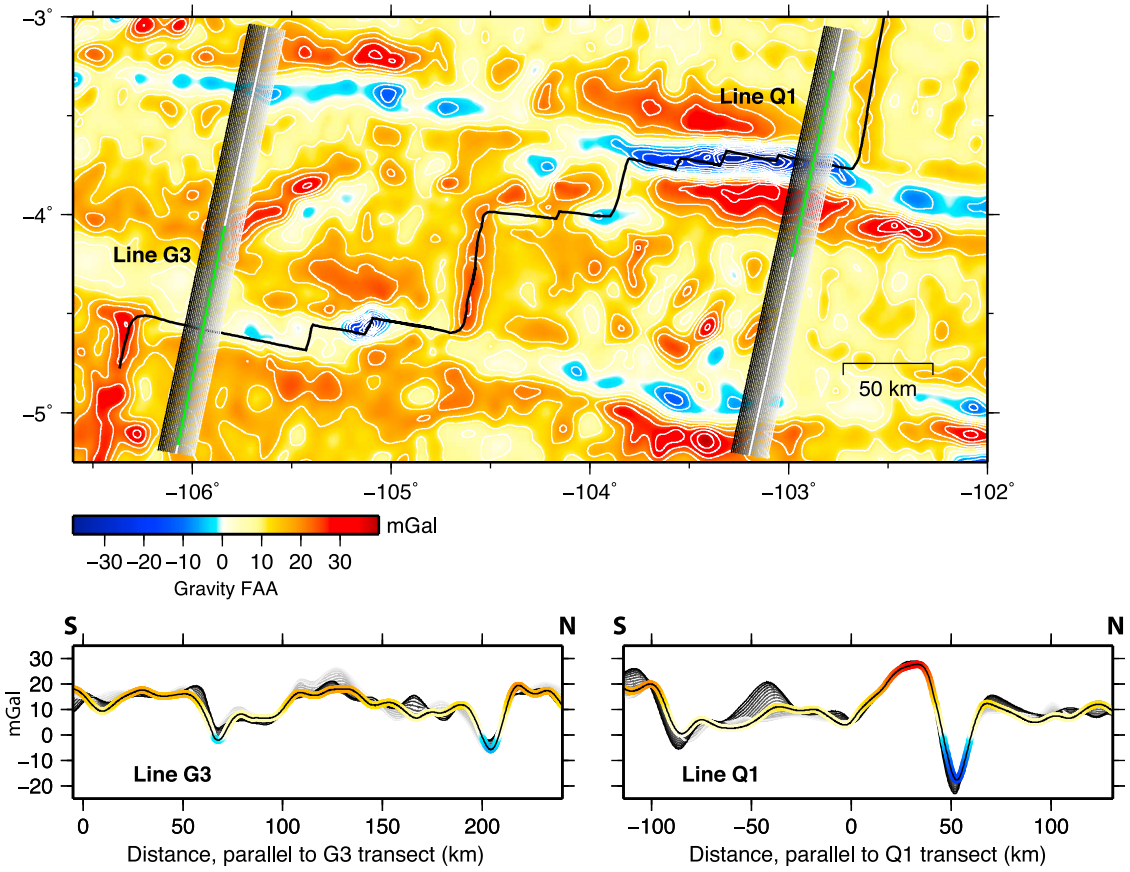

Figure 18. Gravity free-air anomaly, contoured at 5 mGal acquired on the R/V *Knorr* over the QDG fault system from *Pickle et al.* [2009]. (top) Regional map view and (bottom) profiles parallel to the G3 and Q1 lines. Light to dark gray lines in map view show location of gravity profiles drawn in the same color on Figure 18 (bottom), parallel to the tomography line but offset along strike from east to west, to show variation in gravity signature along the fault.

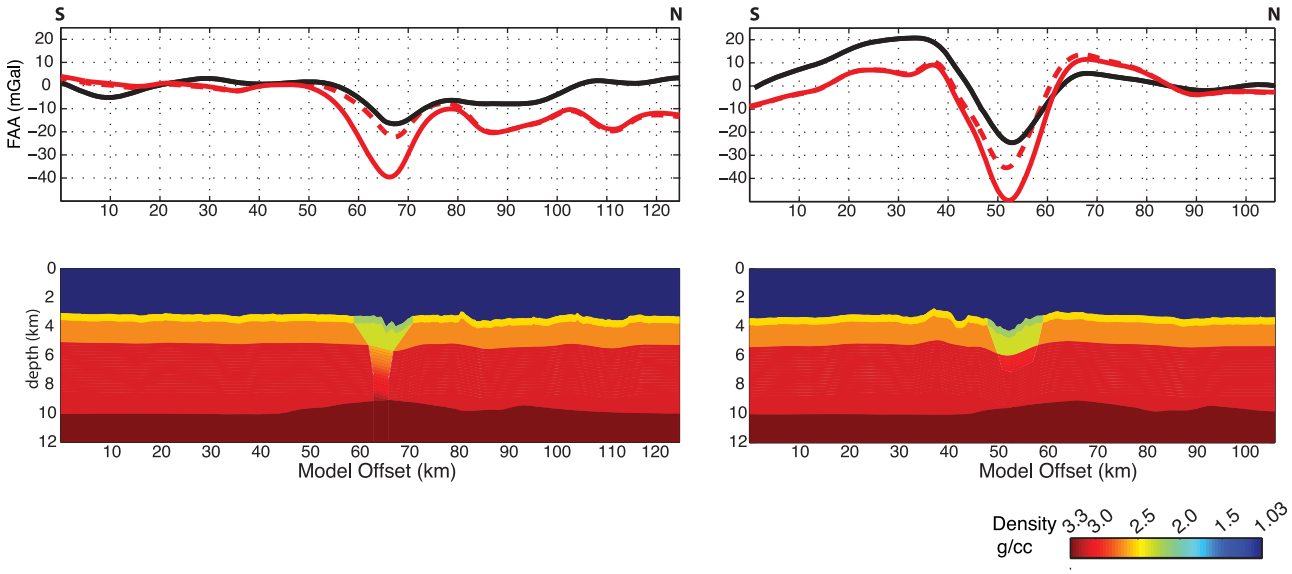

Figure 19. Simple models for the gravity anomaly across the (left) Gofar and (right) Quebrada faults. The predicted gravity anomaly using a reduced density structure is indicated by the solid red lines in Figures 19 (top left) and 19 (top right). Dashed red lines show the gravity anomaly calculated assuming no density contrast in the crust. Black solid lines show the observed free air anomaly. Figures 19 (bottom left) and 19 (bottom right) show crustal density profile and Moho depth used for the gravity anomaly calculations. Fault zone density structure is determined from the seismic velocity structure and the effective media analysis assuming that reduced seismic velocities in the fault zone are caused by the presence of altered peridotite.

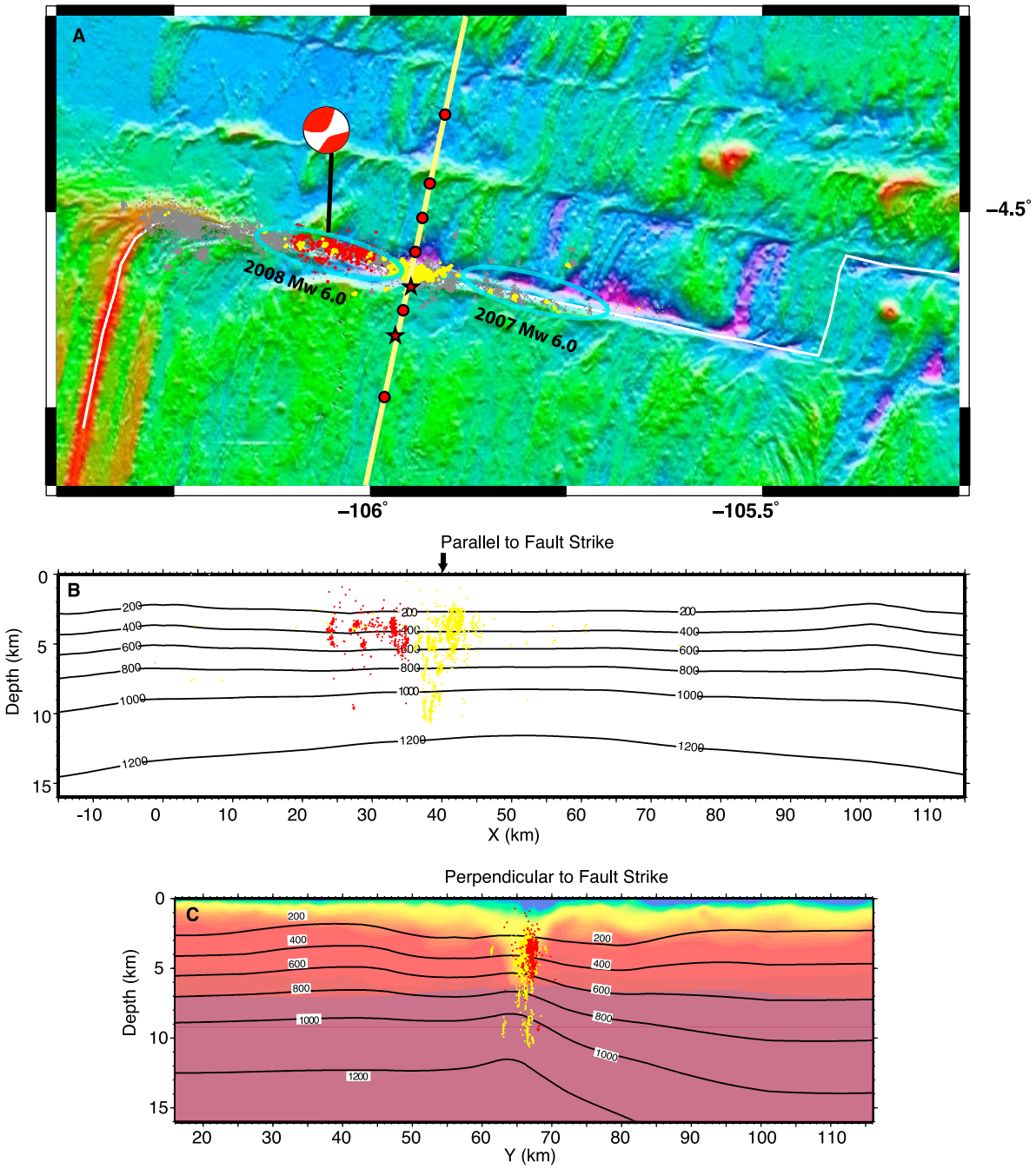

Figure 20. Earthquakes observed during the 2008 OBS deployment on the Gofar fault and isotherms calculated using the numerical model of *Roland et al.* [2010]. (a) Map view of Gofar seismicity and location of G3 refraction transect. Gray dots show earthquakes observed during the yearlong deployment, yellow dots indicate the location of foreshock events that occurred within 1 week before the 2008 M_w 6.0 event, and red dots show the location of aftershocks that occurred within 1 week after the M_w 6.0 event. Cyan ellipses show the approximate extent of the 2007 M_w 6.0 rupture (east) and 2008 M_w 6.0 rupture (west). Plotted focal mechanism is from Global CMT catalog. (b) Depth slice showing same foreshock and aftershocks plotted over isotherms calculated from the 3-D numerical model, along the fault. Numerical thermal models use a simplified Gofar fault geometry (including G1–G3 segments), half spreading rate of 7.0 cm/yr, and simulate hydrothermal cooling with a Nusselt number of 6. (c) Isotherms from the 3-D thermal model plotted perpendicular to the fault and earthquakes projected onto G3 transect. Cross-fault profile (Figure 20c) also shows the seismic velocity model for the G3 transect. Black arrow in Figure 20b shows the approximate location where the refraction transect crosses the fault and the location of cross-fault profile shown in Figure 20c. Earthquakes were located using a double-difference relocation scheme [*McGuire et al.*, 2012].

line is representative of a segment that fails primarily aseismically. In the context of fault mechanics, these results imply that a wide, compliant zone of enhanced fracturing and porosity, and the presence of fluids at seismogenic depths likely contribute to spatial heterogeneity in frictional conditions that influence earthquake behavior and promote variable mechanisms of fault slip at oceanic transform faults.

[55] **Acknowledgments.** Work presented here would not have been possible without the assistance of Alastair Harding, who generously made available the VMTomo code, and provided key input during the writing of this manuscript. This work also benefited hugely from Nathan Miller's expertise in implementing the tomographic inversion framework. Don Forsyth and Robert Pickle provided the gravity data used in the interpretation. High-quality seismic data sets used in this study were acquired with the help of the crew of the R/V *Marcus G. Langseth* and the WHOI OBS team including, Dave Dubois and Peter Lemmond. This manuscript benefited from thoughtful discussions with Margaret Boettcher, Mark Behn, Wenlu Zhu, Greg Hirth, and Stephane Rondenay, as well as from constructive and insightful comments from two anonymous reviewers. The material presented here is based upon work supported by the National Science Foundation Division of Ocean Sciences (OCE) grant 0242117, Division of Earth Sciences (EAR) grant 0943480, and the W. M. Keck Foundation.

References

Abercrombie, R. E., and G. Ekstrom (2001), Earthquake slip on oceanic transform faults, *Nature*, *410*, 74–77, doi:10.1038/35065064.

Anderson, R. N., and R. K. Nishimori (1979), Gabbro, serpentinite, and mafic breccia from the east Pacific, *J. Phys. Earth*, *27*, 467–480, doi:10.4294/jpe1952.27.467.

Avseth, P., T. Mukerji, and G. Mavko (2005), *Quantitative Seismic Interpretation: Applying Rock Physics Tools to Reduce Interpretation Risk*, Cambridge Univ. Press, Cambridge, U. K., doi:10.1017/CBO9780511600074.

Bird, P., Y. Y. Kagan, and D. D. Jackson (2002), Plate tectonics and earthquake potential of spreading ridges and oceanic transform faults, in *Plate Boundary Zones*, *Geodyn. Ser.*, vol. 30, edited by S. Stein and J. T. Freymueller, pp. 203–218, AGU, Washington, D. C., doi:10.1029/GD030p0203.

Boatwright, J., and M. Cocco (1996), Frictional constraints on crustal faulting, *J. Geophys. Res.*, *101*(B6), 13,895–13,909, doi:10.1029/96JB00405.

Boettcher, M. S., and T. H. Jordan (2004), Earthquake scaling relations for mid-ocean ridge transform faults, *J. Geophys. Res.*, *109*, B12302, doi:10.1029/2004JB003110.

Boettcher, M. S., and J. J. McGuire (2009), Scaling relations for seismic cycles on mid-ocean ridge transform faults, *Geophys. Res. Lett.*, *36*, L21301, doi:10.1029/2009GL040115.

Boettcher, M. S., G. Hirth, and B. Evans (2007), Olivine friction at the base of oceanic seismogenic zones, *J. Geophys. Res.*, *112*, B01205, doi:10.1029/2006JB004301.

Bonatti, E. (1976), Serpentinite protrusions in the oceanic crust, *Earth Planet. Sci. Lett.*, *32*(2), 107–113, doi:10.1016/0012-821X(76)90048-0.

Bonatti, E. (1978), Vertical tectonism in oceanic fracture zones, *Earth Planet. Sci. Lett.*, *37*(3), 369–379, doi:10.1016/0012-821X(78)90052-3.

Braunmiller, J., and J. Nábělek (2008), Segmentation of the Blanco Transform Fault Zone from earthquake analysis: Complex tectonics of an oceanic transform fault, *J. Geophys. Res.*, *113*, B07108, doi:10.1029/2007JB005213.

Calvert, A. J., and C. G. Potts (1985), Seismic evidence for hydrothermally altered mantle beneath old crust in the Tydeman fracture zone, *Earth Planet. Sci. Lett.*, *75*(4), 439–449, doi:10.1016/0012-821X(85)90187-6.

Cannat, M., D. Bideau, and R. Hebert (1990), Plastic deformation and magmatic impregnation in serpentinized ultramafic rocks from the Garrett transform fault (East Pacific Rise), *Earth Planet. Sci. Lett.*, *101*(2–4), 216–232, doi:10.1016/0012-821X(90)90155-Q.

Carlson, R. L., and D. J. Miller (2004), Influence of pressure and mineralogy on seismic velocities in oceanic gabbros: Implications for the composition and state of the lower oceanic crust, *J. Geophys. Res.*, *109*, B09205, doi:10.1029/2003JB002699.

Chester, F. M., J. P. Evans, and R. L. Biegel (1993), Internal structure and weakening mechanisms of the San Andreas fault, *J. Geophys. Res.*, *98*(B1), 771–786, doi:10.1029/92JB01866.

Christeson, G. L., G. M. Purdy, and G. J. Fryer (1994), Seismic constraints on shallow crustal emplacement processes at the fast spreading East Pacific Rise, *J. Geophys. Res.*, *99*(B9), 17,957–17,973, doi:10.1029/94JB01252.

Cochran, E. S., Y. G. Li, P. M. Shearer, S. Barbot, Y. Fialko, and J. E. Vidale (2009), Seismic and geodetic evidence for extensive, long-lived fault damage zones, *Geology*, *37*(4), 315–318, doi:10.1130/G25306A.1.

DeMets, C., R. G. Gordon, D. F. Argus, and S. Stein (1990), Current plate motions, *Geophys. J. Int.*, *101*(2), 425–478, doi:10.1111/j.1365-246X.1990.tb06579.x.

Detrick, R. S., and G. M. Purdy (1980), The crustal structure of the Kane fracture zone from seismic refraction studies, *J. Geophys. Res.*, *85*(B7), 3759–3777, doi:10.1029/JB085iB07p03759.

Detrick, R. S., M. H. Cormier, R. A. Prince, D. W. Forsyth, and E. L. Ambos (1982), Seismic constraints on the crustal structure within the Vema Fracture Zone, *J. Geophys. Res.*, *87*(B13), 10,599–10,612, doi:10.1029/JB087iB13p10599.

Detrick, R. S., R. S. White, and G. M. Purdy (1993), Crustal structure of North Atlantic fracture zones, *Rev. Geophys.*, *31*(4), 439–458, doi:10.1029/93RG01952.

Dick, H. J. B., M. A. Tivey, and B. E. Tucholke (2008), Plutonic foundation of a slow-spreading ridge segment: Oceanic core complex at Kane Megamullion, 23°30′N, 45°20′W, *Geochem. Geophys. Geosyst.*, *9*, Q05014, doi:10.1029/2007GC001645.

Eberhart-Phillips, D., W. D. Stanley, B. D. Rodriguez, and W. J. Lutter (1995), Surface seismic and electrical methods to detect fluids related to faulting, *J. Geophys. Res.*, *100*(B7), 12,919–12,936, doi:10.1029/94JB03256.

Fagereng, A. A., and R. H. Sibson (2010), Mélange rheology and seismic style, *Geology*, *38*(8), 751–754, doi:10.1130/G30868.1.

Faulkner, D. R., A. C. Lewis, and E. H. Rutter (2003), On the internal structure and mechanics of large strike-slip fault zones: Field observations of the Carboneras fault in southeastern Spain, *Tectonophysics*, *367*(3–4), 235–251, doi:10.1016/S0040-1951(03)00134-3.

Fialko, Y., D. Sandwell, M. Simons, and P. Rosen (2005), Three-dimensional deformation caused by the Bam, Iran, earthquake and the origin of shallow slip deficit, *Nature*, *435*, 295–299, doi:10.1038/nature03425.

Gregg, P. M., M. D. Behn, J. Lin, and T. L. Grove (2009), Melt generation, crystallization, and extraction beneath segmented oceanic transform faults, *J. Geophys. Res.*, *114*, B11102, doi:10.1029/2008JB006100.

Harding, A. J., J. A. Orcutt, M. E. Kappus, E. E. Vera, J. C. Mutter, P. Buhl, R. S. Detrick, and T. M. Brocher (1989), Structure of young oceanic crust at 13 N on the East Pacific Rise from expanding spread profiles, *J. Geophys. Res.*, *94*(B9), 12,163–12,196, doi:10.1029/JB094iB09p12163.

Hashin, Z., and S. Shtrikman (1963), A variational approach to the theory of the elastic behaviour of multiphase materials, *J. Mech. Phys. Solids*, *11*(2), 127–140, doi:10.1016/0022-5096(63)90060-7.

He, C., Z. Wang, and W. Yao (2007), Frictional sliding of gabbro gouge under hydrothermal conditions, *Tectonophysics*, *445*(3–4), 353–362, doi:10.1016/j.tecto.2007.09.008.

Hébert, R., D. Bideau, and R. Hekinian (1983), Ultramafic and mafic rocks from the Garret Transform Fault near 13°30′S on the East Pacific Rise: Igneous petrology, *Earth Planet. Sci. Lett.*, *65*(1), 107–125, doi:10.1016/0012-821X(83)90193-0.

Hekinian, R., D. Bideau, M. Cannat, J. Francheteau, and R. Hébert (1992), Volcanic activity and crust-mantle exposure in the ultrafast Garrett transform fault near 13°28′S in the Pacific, *Earth Planet. Sci. Lett.*, *108*(4), 259–275, doi:10.1016/0012-821X(92)90027-S.

Houtz, R., and J. Ewing (1976), Upper crustal structure as a function of plate age, *J. Geophys. Res.*, *81*(14), 2490–2498, doi:10.1029/JB081i014p02490.

Iturrino, G. J., N. I. Christensen, S. Kirby, and M. H. Salisbury (1991), Seismic velocities and elastic properties of oceanic gabbroic rocks from Hole 735B, *Proc. Ocean Drill. Program Sci. Results*, *118*, 227–244.

Iturrino, G. J., D. J. Miller, and N. I. Christensen (1996), Velocity behavior of lower crustal and upper mantle rocks from a fast-spreading ridge at Hess Deep, *Proc. Ocean Drill. Program Sci. Results*, *147*, 417–440.

Kaneko, Y., J. P. Avouac, and N. Lapusta (2010), Towards inferring earthquake patterns from geodetic observations of interseismic coupling, *Nat. Geosci.*, *3*(5), 363–369, doi:10.1038/ngeo843.

Korenaga, J., W. S. Holbrook, G. M. Kent, P. B. Kelemen, R. S. Detrick, H. C. Larsen, J. R. Hopper, and T. Dahl-Jensen (2000), Crustal structure of the southeast Greenland margin from joint refraction and reflection seismic tomography, *J. Geophys. Res.*, *105*(B9), 21,591–21,614, doi:10.1029/2000JB900188.

Kosloff, D. D., and E. Baysal (1982), Forward modeling by a Fourier method, *Geophysics*, *47*, 1402–1412, doi:10.1190/1.1441288.

Kuster, G. T., and M. N. Toksöz (1974), Velocity and attenuation of seismic waves in two-phase media; Part I, Theoretical formulations, *Geophysics*, *39*(5), 587–606, doi:10.1190/1.1440450

Langmuir, C., and D. W. Forsyth (2007), Mantle melting beneath mid-ocean ridges, *Oceanography*, *20*, 78–89, doi:10.5670/oceanog.2007.82.

Lewis, M. A., Y. Ben-Zion, and J. J. McGuire (2007), Imaging the deep structure of the San Andreas Fault south of Hollister with joint analysis

of fault zone head and direct P arrivals, *Geophys. J. Int.*, *169*(3), 1028–1042, doi:10.1111/j.1365-246X.2006.03319.x.

Liu, Y., and A. M. Rubin (2010), Role of fault gouge dilatancy on aseismic deformation transients, *J. Geophys. Res.*, *115*, B10414, doi:10.1029/2010JB007522.

Marone, C. (1998), Laboratory-derived friction laws and their application to seismic faulting, *Annu. Rev. Earth Planet. Sci.*, *26*(1), 643–696, doi:10.1146/annurev.earth.26.1.643.

Marone, C., and B. Kilgore (1993), Scaling of the critical slip distance for seismic faulting with shear strain in fault zones, *Nature*, *362*, 618–621, doi:10.1038/362618a0.

Marone, C., and C. H. Scholz (1988), The depth of seismic faulting and the upper transition from stable to unstable slip regimes, *Geophys. Res. Lett.*, *15*(6), 621–624, doi:10.1029/GL015i006p00621.

Marone, C., M. Cocco, E. Richardson, and E. Tinti (2009), The critical slip distance for seismic and aseismic fault zones of finite width, *Int. Geophys.*, *94*, 135–162, doi:10.1016/S0074-6142(08)00006-5.

McGuire, J. J. (2008), Seismic cycles and earthquake predictability on East Pacific Rise transform faults, *Bull. Seismol. Soc. Am.*, *98*(3), 1067–1084, doi:10.1785/0120070154.

McGuire, J. J., J. A. Collins, P. Gouédard, E. Roland, D. Lizarralde, M. S. Boettcher, M. D. Behn, and R. D. van der Hilst (2012), Variations in earthquake rupture properties along the Gofar transform fault, East Pacific Rise, *Nat. Geosci.*, *5*(5), 336–341, doi:10.1038/ngeo1454.

Michael, A. J., and D. Eberhart-Phillips (1991), Relations among fault behavior, subsurface geology, and three-dimensional velocity models, *Science*, *253*(5020), 651–654, doi:10.1126/science.253.5020.651.

Miller, D. J., and N. I. Christensen (1997), Seismic velocities of lower crustal and upper mantle rocks from the slow-spreading Mid-Atlantic Ridge, south of the Kane Transform Zone (MARK), *Proc. Ocean Drill. Program Sci. Results*, *153*, 437–454. [Available at http://cat.inist.fr/?aModele=afficheN&cpsidt=2817434.]

Minshull, T. A., R. S. White, J. C. Mutter, P. Buhl, R. S. Detrick, C. A. Williams, and E. Morris (1991), Crustal structure at the Blake Spur Fracture Zone from expanding spread profiles, *J. Geophys. Res.*, *96*(B6), 9955–9984, doi:10.1029/91JB00431.

Moore, D. E., and D. A. Lockner (2007), Comparative deformation behavior of minerals in serpentinized ultramafic rock: Application to the slab-mantle interface in subduction zones, *Int. Geol. Rev.*, *49*(5), 401–415, doi:10.2747/0020-6814.49.5.401.

Moore, D. E., D. A. Lockner, M. Shengli, R. Summers, and J. D. Byerlee (1997), Strengths of serpentinite gouges at elevated temperatures, *J. Geophys. Res.*, *102*(B7), 14,787–14,801, doi:10.1029/97JB00995.

Moser, T. J., G. Nolet, and R. Snieder (1992a), Ray bending revisited, *Bull. Seismol. Soc. Am.*, *82*(1), 259–288.

Moser, T. J., T. Van Eck, and G. Nolet (1992b), Hypocenter determination in strongly heterogeneous earth models using the shortest path method, *J. Geophys. Res.*, *97*(B5), 6563–6572, doi:10.1029/91JB03176.

Nagle, A. N., A. Saal, R. C. Pickle, D. W. Forsyth, and S. R. Hart (2009), Two-component Mixing in MORB: Evidence from the Quebrada-Discovery-Gofar Fracture Zone (EPR 3°–5°S), *Eos Trans. AGU*, *90*(52), Fall Meet. Suppl., Abstract V31D-1985.

Pickle, R. C., D. W. Forsyth, N. Harmon, A. N. Nagle, and A. Saal (2009), Thermo-mechanical control of axial topography of intra-transform spreading centers, *Earth Planet. Sci. Lett.*, *284*(3–4), 343–351, doi:10.1016/j.epsl.2009.05.004.

Purdy, G. M. (1987), New observations of the shallow seismic structure of young oceanic crust, *J. Geophys. Res.*, *92*(B9), 9351–9361, doi:10.1029/JB092iB09p09351.

Reinen, L. A. (2000), Seismic and aseismic slip indicators in serpentinite gouge, *Geology*, *28*(2), 135–138, doi:10.1130/0091-7613(2000)28<135:SAASII>2.0.CO;2.

Roland, E., and J. J. McGuire (2009), Earthquake swarms on transform faults, *Geophys. J. Int.*, *178*(3), 1677–1690, doi:10.1111/j.1365-246X.2009.04214.x.

Roland, E., M. D. Behn, and G. Hirth (2010), Thermal-mechanical behavior of oceanic transform faults: Implications for the spatial distribution of seismicity, *Geochem. Geophys. Geosyst.*, *11*, Q07001, doi:10.1029/2010GC003034.

Saal, A. E., and D. W. Forsyth (2004), MORB composition in intra-transform spreading centers: A key test of models of mantle flow and melt transport, *Eos Trans. AGU*, *85*(47), Fall Meet. Suppl., Abstract T12A-04.

Savage, H. M., and E. E. Brodsky (2011), Collateral damage: Evolution with displacement of fracture distribution and secondary fault strands in fault damage zones, *J. Geophys. Res.*, *116*, B03405, doi:10.1029/2010JB007665.

Schulz, S. E., and J. P. Evans (2000), Mesoscopic structure of the Punchbowl Fault, Southern California and the geologic and geophysical structure of active strike-slip faults, *J. Struct. Geol.*, *22*(7), 913–930, doi:10.1016/S0191-8141(00)00019-5.

Searle, R. (1983), Multiple, closely spaced transform faults in fast-slipping fracture zones, *Geology*, *11*(10), 607–610, doi:10.1130/0091-7613(1983)11<607:MCSTFI>2.0.CO;2.

Segall, P., and A. M. Bradley (2012), The role of thermal pressurization and dilatancy in controlling the rate of fault slip, *J. Appl. Mech.*, *79*(3), 031013, doi:10.1115/1.4005896.

Segall, P., and J. Rice (1995), Dilatancy, compaction, and slip instability of a fluid infiltrated fault, *J. Geophys. Res.*, *100*(101), 22,155–22,171, doi:10.1029/95JB02403.

Segall, P., A. M. Rubin, A. M. Bradley, and J. R. Rice (2010), Dilatant strengthening as a mechanism for slow slip events, *J. Geophys. Res.*, *115*, B12305, doi:10.1029/2010JB007449.

Shearer, P. (1999), *Introduction to Seismology*, Cambridge Univ. Press, Cambridge, U. K.

Shearer, P. M. (2002), Parallel fault strands at 9-km depth resolved on the Imperial Fault, southern California, *Geophys. Res. Lett.*, *29*(14), 1674, doi:10.1029/2002GL015302.

Thurber, C., S. Roecker, W. Ellsworth, Y. Chen, W. Lutter, and R. Sessions (1997), Two-dimensional seismic image of the San Andreas Fault in the northern Gabilan Range, central California: Evidence for fluids in the fault zone, *Geophys. Res. Lett.*, *24*(13), 1591–1594, doi:10.1029/97GL01435.

Thurber, C., H. Zhang, F. Waldhauser, J. Hardebeck, A. Michael, and D. Eberhart-Phillips (2006), Three-dimensional compressional wavespeed model, earthquake relocations, and focal mechanisms for the Parkfield, California, region, *Bull. Seismol. Soc. Am.*, *96*(4B), S38, doi:10.1785/0120050825.

Toomey, D., and G. Foulger (1989), Tomographic Inversion of Local Earthquake Data From the Hengill-Grensdalur Central Volcano Complex, Iceland, *J. Geophys. Res.*, *94*(B12), 17,497–17,510, doi:10.1029/JB094iB12p17497.

Toomey, D. R., S. C. Solomon, and G. M. Purdy (1994), Tomographic imaging of the shallow crustal structure of the East Pacific Rise at 9°30′N, *J. Geophys. Res.*, *99*(B12), 24,135–24,157, doi:10.1029/94JB01942.

Tréhu, A. M., and G. M. Purdy (1984), Crustal structure in the Orozco transform zone, *J. Geophys. Res.*, *89*(B3), 1834–1842, doi:10.1029/JB089iB03p01834.

Tucholke, B. E., and J. Lin (1994), A geological model for the structure of ridge segments in slow spreading ocean crust, *J. Geophys. Res.*, *99*(B6), 11,937–11,958, doi:10.1029/94JB00338.

Van Avendonk, H. J. (1998), An investigation of the crustal structure of the Clipperton transform fault area using 3 D seismic tomography, thesis, Univ. of Calif., San Diego.

Van Avendonk, H. J., A. J. Harding, J. A. Orcutt, and J. S. McClain (1998), A two-dimensional tomographic study of the Clipperton transform fault, *J. Geophys. Res.*, *103*(B8), 17,885–17,899, doi:10.1029/98JB00904.

Van Avendonk, H. J. A., A. J. Harding, J. A. Orcutt, and J. S. McClain (2001), Contrast in crustal structure across the Clipperton transform fault from travel time tomography, *J. Geophys. Res.*, *106*(B6), 10,961–10,981, doi:10.1029/2000JB900459.

Van Avendonk, H. J. A., D. J. Shillington, W. S. Holbrook, and M. J. Hornbach (2004), Inferring crustal structure in the Aleutian island arc from a sparse wide-angle seismic data set, *Geochem. Geophys. Geosyst.*, *5*, Q08008, doi:10.1029/2003GC000664.

Vera, E. E., J. C. Mutter, P. Buhl, J. A. Orcutt, A. J. Harding, M. E. Kappus, R. S. Detrick, and T. M. Brocher (1990), The structure of 0-to 0.2-my-old oceanic crust at 9 N on the East Pacific Rise from expanded spread profiles, *J. Geophys. Res.*, *95*(B10), 15,529–15,556, doi:10.1029/JB095iB10p15529.

Wei, M., D. Sandwell, and Y. Fialko (2009), A silent M_w 4.7 slip event of October 2006 on the Superstition Hills fault, southern California, *J. Geophys. Res.*, *114*, B07402, doi:10.1029/2008JB006135.

Wendt, J. I., M. Regelous, Y. Niu, R. Hékinian, and K. D. Collerson (1999), Geochemistry of lavas from the Garrett Transform Fault: Insights into mantle heterogeneity beneath the eastern Pacific, *Earth Planet. Sci. Lett.*, *173*(3), 271–284, doi:10.1016/S0012-821X(99)00236-8.

Wessel, P., and W. F. Haxby (1990), Thermal stresses, differential subsidence, and flexure at oceanic fracture zones, *J. Geophys. Res.*, *95*(B1), 375–391, doi:10.1029/JB095iB01p00375.

White, R. S., R. S. Detrick, M. C. Sinha, and M. H. Cormier (1984), Anomalous seismic crustal structure of oceanic fracture zones, *Geophys. J. R. Astron. Soc.*, *79*(3), 779–798, doi:10.1111/j.1365-246X.1984.tb02868.x.

White, R. S., D. McKenzie, and R. K. O'Nions (1992), Oceanic crustal thickness from seismic measurements and rare earth element inversions, *J. Geophys. Res.*, *97*(B13), 19,683–19,715, doi:10.1029/92JB01749.

Wilcock, W. S., G. M. Purdy, and S. C. Solomon (1990), Microearthquake evidence for extension across the Kane transform fault, *J. Geophys. Res.*, *95*(B10), 15,439–15,462, doi:10.1029/JB095iB10p15439.